Emergent complexity and rhythms in evoked and spontaneous dynamics of human whole-brain models after tuning through analysis tools

Gianluca Gaglioti[a,b,1,*], Alessandra Cardinale[c,d,1], Cosimo Lupo[d], Thierry Nieus[e], Federico Marmoreo[d], Robin Gutzen[f], Michael Denker[g], Andrea Pigorini[h,i], Marcello Massimini[a,j,k,2], Simone Sarasso[a,2], Pier Stanislao Paolucci[d,2], Giulia De Bonis[d,2]

[a]*Dep. of Biomedical and Clinical Sciences, Univ. of Milan, Milan, , Italy*
[b]*Dep. of Philosophy "Piero Martinetti", Univ. of Milan, Milan, , Italy*
[c]*Università Campus Bio-medico di Roma, Rome, 00128, Italy*
[d]*Istituto Nazionale di Fisica Nucleare (INFN), Sezione di Roma, Rome, 00185, Italy*
[e]*Dep. Environmental Science and Policy, Univ. of Milan, Milan, , Italy*
[f]*Center for Data Science, New York University, New York, , U.S.A.*
[g]*Institute for Advanced Simulation (IAS-6), Jülich Research Centre, Jülich, , Germany*
[h]*Dep. of Biomedical, Surgical and Dental Sciences, Univ. of Milan, Milan, , Italy*
[i]*UOC Maxillo-facial Surgery and dentistry, Fondazione IRCCS Cà Granda, Ospedale Maggiore Policlinico, Milan, , Italy*
[j]*IRCCS Fondazione Don Carlo Gnocchi ONLUS, Milan, , Italy*
[k]*Azrieli Program in Brain, Mind and Consciousness, Canadian Institute for Advanced Research, Toronto, , Canada*

Abstract

The simulation of whole-brain dynamics should reproduce realistic spontaneous and evoked neural activity across different scales, including emergent rhythms, spatio-temporal activation patterns, and macroscale complexity. Once a mathematical model is selected, its configuration must be determined by properly setting its parameters. A critical preliminary step in this process is defining an appropriate set of observables to guide the selection of model configurations (parameter tuning), laying the groundwork for quantitative calibration of accurate whole-brain models. Here, we address this challenge by presenting a framework that integrates two complementary tools: The Virtual Brain (TVB) platform for simulating whole-brain dynamics, and the Collaborative Brain Wave Analysis Pipeline (Cobrawap) for analyzing the simulations using a set of standardized metrics. We apply this framework to a 998-node human connectome, using two configurations of the Larter-Breakspear neural mass model: one with the TVB default parameters, the other tuned using Cobrawap. The results

1

reveal that the tuned configuration exhibits several biologically relevant features, absent in the default model for both spontaneous and evoked dynamics. In response to external perturbations, the tuned model generates non-stereotyped, complex spatio-temporal activity, as measured by the perturbational complexity index. In spontaneous activity, it displays robust alpha-band oscillations, infra-slow rhythms, scale-free characteristics, greater spatio-temporal heterogeneity, and asymmetric functional connectivity. This work demonstrates the potential of combining TVB and Cobrawap to guide parameter tuning and lays the groundwork for data-driven calibration and validation of accurate whole-brain models.

Keywords: whole-brain simulations, emergent complexity, brain rhythms, model tuning, human connectome, Larter-Breakspear model

1. Introduction

Whole-brain computational models based on the neural mass approximation provide a framework for investigating the fundamental mechanisms underlying large-scale neural dynamics (Breakspear, 2017; Griffiths et al., 2022). However, a crucial challenge remains: how to configure and adjust such a model so that it simultaneously captures key features of spontaneous and evoked brain activity, and ultimately calibrate it to match empirical data.

Among the essential features that a biologically realistic whole-brain model should reproduce, the alpha rhythm (8–12 Hz) stands out as a fundamental oscillation in large-scale brain dynamics. First described by Berger (1929), it is closely associated with states of relaxed wakefulness and is thought to play a role in cognitive processes (Klimesch, 1999; Jensen and Mazaheri, 2010). While alpha oscillations are a hallmark of resting-state dynamics, their fluctuating and multistable nature reflects the inherent variability and the transient state shifts of the brain (Freyer et al., 2009, 2011). In addition, they do not act in isolation but rather coexist with fluctuations occurring across multiple timescales (Fox and Raichle, 2007; Palva and Palva, 2012). At rest, brain activity fluctuates over time, exhibiting complex

---

*Corresponding author: gaglioti.gianluca@gmail.com

[1] These authors contributed equally.

[2] These authors jointly supervised this work.

patterns of spontaneous variation in neuronal signals shaping the functional organization of the brain (Deco et al., 2017). Fluctuations also exhibit significant regional heterogeneity, with varying degrees of signal variability influenced by anatomical connectivity and functional roles (Deco et al., 2011). High-fluctuation regions act as integrative hubs, crucial for coordinating information flow across the network (Rabuffo et al., 2021; van den Heuvel and Sporns, 2013). These regions may contribute to infra-slow fluctuations ($< 0.1\,\mathrm{Hz}$), which shape large-scale brain dynamics (Palva and Palva, 2012; Gutierrez-Barragan et al., 2019; Rabuffo et al., 2021; Väyrynen et al., 2023) and drive dynamic functional connectivity and brain state reconfiguration (Tagliazucchi et al., 2012; Gutierrez-Barragan et al., 2019). Beyond this spontaneous dynamics, the awake brain also exhibits sustained and spatially complex responses evoked by external focal perturbations, a phenomenon that has been extensively studied in experimental settings, such as in transcranial magnetic stimulation combined with simultaneous electroencephalography (TMS-EEG) experiments, where the spatio-temporal complexity of the evoked cortical response has been shown to correlate with the level of consciousness (Rosanova et al., 2012; Casali et al., 2013; Casarotto et al., 2016). These features – multistability, scale-free and infra-slow fluctuations, dynamic reconfiguration, and complex evoked responses – have been increasingly linked to critical dynamics in the brain (Deco and Jirsa, 2012; O'Byrne and Jerbi, 2022). The hypothesis of brain criticality posits that neural systems operate near a critical point between order and disorder, a regime that supports maximal variability, long-range correlations, and optimal responsiveness to external inputs (Beggs and Plenz, 2003; Chialvo, 2010; Shew and Plenz, 2012; Cocchi et al., 2017; Palva and Palva, 2018; Maschke et al., 2024).

A key question emerging from these considerations is whether a single, unified model can simultaneously reproduce both features of spontaneous and evoked brain activity. Indeed, traditionally, these two have been treated as separate problems in computational modeling. However, a relationship is expected between the richness of spontaneous activity patterns and the brain's ability to sustain complex responses to external perturbations through its network dynamics. Addressing this interplay requires an initial parameter tuning, aimed at exploring how changes in model settings impact on defined features, followed by a calibration

of model parameters against a set of defined features and constraints so to ensure that the model captures the brain broader dynamical landscape, beyond the reproduction of isolated features. Finally, a more thorough validation must be performed against a range of statistical features to establish their agreement with respect to experimental data (e.g., Trensch et al., 2018; Gutzen et al., 2018).
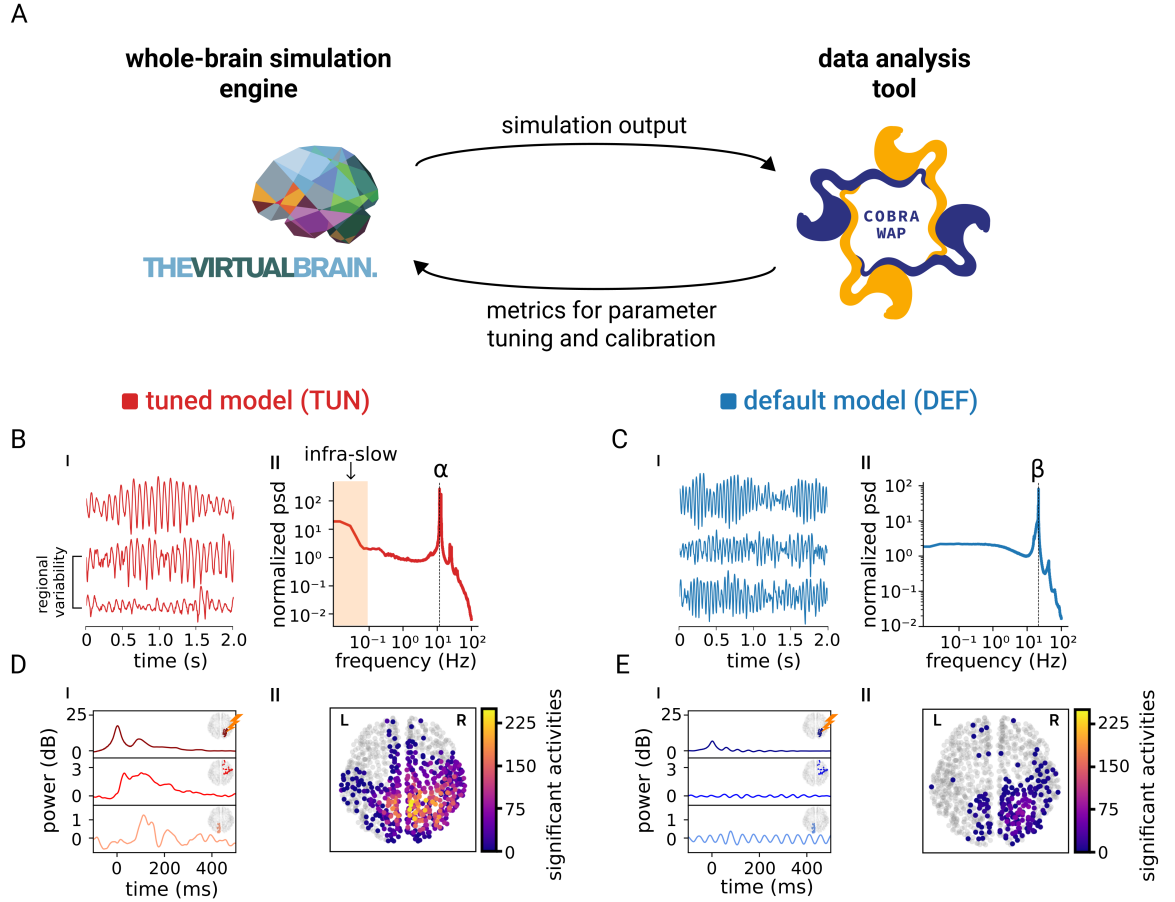

Figure 1: **TVB simulations and analysis with Cobrawap.**

A) The TVB-Cobrawap workflow facilitates tuning, calibration and validation of TVB model parameters. Cobrawap provides metrics for the analysis of TVB outputs such as trace statistics, event detection, spectral analysis, network interactions, and complexity indexes of simulated brain activity. **B)** Illustrative examples of three spontaneous activity traces from three cortical regions of the tuned (TUN) configuration (B_I). These represent proxies of synaptic activity, obtained by convolving the voltage traces with a bi-exponential kernel (see Sec. 2.5.2) at the single-node level, and subsequently averaging the resulting signals across nodes belonging to each region. From top to bottom, the traces correspond to the average synaptic activity across

left-hemisphere nodes belonging to the IP, IT, and PARC regions, respectively (see Tab. A.1). The average Power Spectral Density (PSD) across all regions displays a clear peak in the alpha band, at approximately 12 Hz, together with an enriched infra-slow spectral component (B_{II}). **C)** Same as B), referred to the default (DEF) configuration. In this case, the dominant peak in the PSD is observed within the beta frequency band, centered around 21.6 Hz, with no relevant infra-slow activity. **D-E)** A brief stimulus (2 ms) was applied to the same nodes of the TUN and DEF configurations, to assess the spatio-temporal propagation of evoked activity. The post-stimulus power (see Sec. 2.5.3) of three subsets of nodes (specifically, the subset of stimulated nodes, a subset of far nodes connected to the stimulated nodes but in the same hemisphere where stimulation occurred, and the farthest set of nodes – in terms of connectome tracts – connected to the stimulated nodes), averaged across the same subset, displayed a consistent increase in all subsets in the TUN configuration with respect to DEF, together with a higher heterogeneity in the temporal evolution (compare D_I with E_I). The extent of significant post-stimulus activity (see Sec. 2.5.5), computed by summing the significant activity of each node between 10 and 500 ms, was mapped onto the brain map for TUN (D_{II}) and DEF (E_{II}). The panels indicate a more widespread propagation in TUN compared to DEF.

To assess the consistency of a model with empirical data, the challenge is to define appropriate *metrics* (i.e., numbers providing a quantitative characterization of an observation) for guiding the calibration process (i.e., adjusting parameters to optimally match a given dataset) and for validating model plausibility (i.e., testing the calibrated model with new data, e.g., from different brain states or subjects). When discrepancies occur, these metrics offer feedback for refining the model and identifying its region of applicability, thereby improving rigor and generalizability in its ability to replicate real neural dynamics. To enhance reproducibility, leverage the wealth of heterogeneous data available and facilitate cross-study comparisons, these metrics should be accessible to the broader neuroscientific community and sufficiently general and cross-validated to embrace a wide range of case studies. Ensuring such broad adoption and methodological consistency is particularly important when calibrating and validating computational models, as it enables a more precise alignment between theoretical predictions and experimental observations. Likewise, the model description and simulation should be standardized across the calibration/validation loops and must be carried out by a robust simulation workflow.

A number of frameworks address these needs for standardization both for simulation

and data analytics. Platforms like The Virtual Brain (TVB) (Sanz-Leon et al., 2013, 2015), Neurolib (Cakan et al., 2023), and the Brain Dynamics Toolbox (Heitmann et al., 2018) facilitate and standardize whole-brain simulations using neural mass models, which describe large-scale neural interactions via phenomenological or mean-field approaches (Breakspear, 2017). Among the advantages of these solutions, the prebuilt, validated models offered by these platforms streamline calibration against empirical data, allowing researchers to focus on scientific questions rather than custom coding. Active user communities further enhance reproducibility and collaboration. Standardized data analysis workflows that ensure reproducible analysis are supported by tools like MNE (Gramfort et al., 2013) for EEG/MEG, FreeSurfer (Fischl, 2012) for Magnetic Resonance Imaging (MRI), fMRIPrep (Esteban et al., 2019) for functional MRI (fMRI), and Elephant (Denker et al., 2018) for electrophysiological data. Such methodologies integrate heterogeneous data, minimize inconsistencies, and enhance comparability, crucial for addressing the challenges of multimodal neuroscience. Extending this principle to complete analytics workflows, the Collaborative Brain Wave Analysis Pipeline (Cobrawap) (Gutzen et al., 2024, 2025a) is developed as an open-source tool providing standardized and quantitative descriptions of brain wave phenomena, addressing the growing need for shared and agreed metrics and methodologies in the field. Complementing this ecosystem of tools, broad initiatives like EBRAINS (EBRAINS: Europe Research Infrastructure for Brain Research, 2023), the Allen Brain Atlas (Sunkin et al., 2013), and the Human Connectome Project (Van Essen et al., 2012) provide shared curated data and frameworks.

In this study, we took the first steps toward the calibration of a whole-brain model able to simultaneously reproduce key features of both spontaneous and evoked brain dynamics. To this end, we employed a recently developed whole-brain model implemented in TVB (Gaglioti et al., 2024) and identified the most relevant parameters to be tuned, following an iterative approach (Fig. 1A). Leveraging analysis methods implemented in Cobrawap, we extracted metrics about relevant features of the whole-brain model: alpha-band oscillations, infra-slow fluctuations, and the spatio-temporal complexity of evoked responses. By varying the related parameters, we could drive the model simulations into activity regimes that

show more similarities to the heterogeneous, multiscale features of large-scale brain activity. Hence, our results show that a tuned model can account for both the variability of resting-state activity and the complexity of stimulus-evoked responses, thus bridging a gap between traditionally separate modeling efforts for the two conditions. Moreover, we set the ground for generalizable validation metrics provide a robust foundation for future empirical testing and integration into automated classification workflows.

2. Materials and Methods

In the following, we first detail the TVB implementation of the whole-brain model to be later tuned, followed by a description of the analysis steps used for measuring model features and performances.

2.1. Model equations

We used the Larter-Breakspear (LB) model (Larter et al., 1999; Breakspear and Terry, 2002; Breakspear et al., 2003; Breakspear and Stam, 2005), a voltage-based phenomenological neural mass model commonly used to simulate whole-brain activity (Honey et al., 2007; Honey and Sporns, 2008; Alstott et al., 2009; Honey et al., 2009; Gollo and Breakspear, 2014; Gollo et al., 2015; Roberts et al., 2019; Endo et al., 2020; Gaglioti et al., 2024), implemented within the TVB simulator. Connectivity was implemented by means of a 998-node bi-hemispherical connectome (Hagmann et al., 2008), where each node represents a source of signal reproducing the spontaneous dynamics of a neural mass model in the resting state.

The dynamics of a given node in the brain network is described by the following set of ordinary differential equations:

$$\frac{1}{t_{\text{scale}}} \frac{dV}{dt} = - \left[g_{\text{Ca}} + (1 - C) r_{\text{NMDA}} \, a_{e \to e} \, Q_V + C \, r_{\text{NMDA}} \, a_{e \to e} \, Q_{V,\text{network}} \right] m_{\text{Ca}} (V - V_{\text{Ca}})$$

$$- \left[g_{\text{Na}} \, m_{\text{Na}} + (1 - C) \, a_{e \to e} \, Q_V + C \, a_{e \to e} \, Q_{V,\text{network}} \right] (V - V_{\text{Na}})$$

$$- g_{\text{K}} W (V - V_{\text{K}}) - g_{\text{L}} (V - V_{\text{L}}) - a_{i \to e} Z Q_Z + a_{n \to e} I + \xi_V \, ,$$

$$(1a)$$

$$\frac{1}{t_{\text{scale}}} \frac{dZ}{dt} = b \, (a_{n \to i} I + a_{i \to e} Q_V V) + \xi_Z \, , \tag{1b}$$

$$\frac{1}{t_{\text{scale}}} \frac{dW}{dt} = \frac{\phi \, (m_{\text{K}} - W)}{\tau_{\text{K}}} + \xi_W \, , \tag{1c}$$

where V and Z are the mean membrane potential of the excitatory pyramidal neurons and inhibitory interneurons for that node, respectively, while W corresponds to the average number of open potassium (K) channels. The term t_{scale} is an adimensional time-scaling factor that rescales the temporal dynamics of all state variables. The ratio of NMDA receptors to AMPA receptors is captured by r_{NMDA}, and $a_{x \to y}$ defines the synaptic strength between source population x (where x is one of e: excitatory, i: inhibitory, or n: nonspecific input) and target population y (where y is e or i). I represents an external input current, modeling nonspecific excitatory drive, such as subcortical or thalamic inputs, that influences the activity of excitatory (V) and inhibitory (Z) populations. The dynamics of Z and W are governed by the constant rate terms b, τ_{K} and ϕ, which respectively represent a time constant for inhibitory activity (Z), a time constant for W relaxation, and a temperature scaling factor for the evolution of W.

For each ion species, g_{ion} (where ion is one of Ca: calcium, Na: sodium, or K: potassium) represents the maximum ion conductance and V_{ion} represents its reversal potential. Similarly, g_{L} and V_{L} represent the maximum leakage conductance and reversal potential, respectively. The voltage-dependent fraction of open channels is governed by m_{ion}, following a sigmoidal

shape function for each node:

$$m_{\text{ion}}(t) = \frac{1}{2}\left[1 + \tanh\left(\frac{V(t) - T_{\text{ion}}}{\delta_{\text{ion}}}\right)\right],\tag{2}$$

where T_{ion} term represents the mean threshold membrane potential for a given ion channel population, while δ_{ion} denotes its standard deviation. The mean firing rates of the excitatory and inhibitory node populations are governed by the voltage-dependent activation functions Q_{V} and Q_{Z}, respectively, which are modeled as sigmoidal as well:

$$Q_{\text{V}}(t) = \frac{1}{2}Q_{\text{V}_{\max}}\left[1 + \tanh\left(\frac{V(t) - V_{\text{T}}}{\delta_{\text{V}}}\right)\right],\tag{3a}$$

$$Q_{\text{Z}}(t) = \frac{1}{2}Q_{\text{Z}_{\max}}\left[1 + \tanh\left(\frac{Z(t) - Z_{\text{T}}}{\delta_{\text{Z}}}\right)\right],\tag{3b}$$

where the terms $Q_{\text{V}_{\max}}$ and $Q_{\text{Z}_{\max}}$ are the maximum firing rates of the excitatory and inhibitory population, respectively. The thresholds for action potential generation for these populations are given by V_{T} and Z_{T}, with corresponding standard deviations δ_{V} and δ_{Z}, respectively. Finally, the input to a node k coming from the rest of the network, $Q_{\text{V,network}}^{(k)}$, is defined as:

$$Q_{\text{V,network}}^{(k)}(t) = G\sum_{\{j\}} u_{j\to k}\, Q_{\text{V}}^{(j)}(t - \tau_{j\to k})\,,\tag{4}$$

with the sum running over all the nodes $\{j\}$ connected to k with connection weight $u_{j\to k}$, and $\tau_{j\to k}$ denoting the related input delay time. G is the global coupling that scales all the connection weights. The parameter C in Eq. (1) varies between 0 and 1 and controls the balance between the strength of self-connections and the connections with the rest of the network. Finally, an additive Gaussian noise ξ (with standard deviation 10^{-7}) enters in Eq. (1) through the stochastic Heun integration method of TVB.

2.2. Model configurations and parameters

We implemented two parameter configurations for the LB model, with their values fully listed in Tab. A.2. The first configuration, referred to as the tuned configuration (TUN) from here on, is based on the work by Gaglioti et al. (2024), with some further refinements here. The second configuration, derived from the default parameters in TVB, follows the work of Alstott et al. (2009) and will be referred to as the default configuration (DEF). The TUN configuration is capable of generating complex evoked patterns following external stimulation (Gaglioti et al., 2024), resembling empirical results from the healthy awake brain. In this study, we focused on resting-state activity and, to better approach empirical data, we adjusted the timescale of the TUN configuration (see Tab. A.2) to reproduce the alpha-band location of the experimentally observed peak in the power spectrum of the global resting state activity (Berger, 1929; Klimesch, 1999; Jensen and Mazaheri, 2010). Consistently, the TUN configuration exhibited a peak at 11.7 Hz in the resting condition (Fig. 1B) and displayed complex dynamics following perturbation (Fig. 1D; see the following section for further details on the simulation of resting-state and evoked activity). The corresponding measures for the DEF configuration are depicted in Figs. 1C and 1E, respectively.

2.3. Model activity simulation in TVB

Each simulation was run in TVB (RRID:SCR_002249) with a time step of $\delta_t = 0.1$ ms using the stochastic Heun integration method. A Gaussian white noise was added to the state variables to emulate an additional input at the "background" of the node (standard deviation $\sigma_\xi = 10^{-7}$ for the DEF configuration, then rescaled by t_{scale} for TUN). The signal was then resampled to a temporal resolution of 1 ms (i.e., averaging over 1 ms time windows with the *temporal average monitor* of TVB).

For resting state, five minutes of continuous brain activity were simulated. Initial conditions were randomly assigned, with the values of the state variables (V, Z, W) drawn from a uniform distribution between -0.1 and 0.1. A conservative choice was made based on the observation that the initial transient phenomenon is concluded after roughly 5 s, hence an initial period of 10 s was excluded.

For evoked activity, 200 trials were simulated. A stimulus of 1 arbitrary unit (a.u.) in amplitude and 2 ms in duration was applied to the 27 nodes belonging to the right superior parietal (rSP) cortex region. Each trial began with random initial conditions. The onset timing of the stimulus was randomized within a window between 10 s and 12 s, so again allowing for a long enough thermalization period after the random initialization. Finally, we retained 400 ms of pre-stimulus activity (baseline) and 700 ms of post-stimulus activity.

2.4. Tuning TVB model parameters with Cobrawap

We utilized the Cobrawap framework (RRID: SCR_022966; (Gutzen et al., 2025a,b)) to implement the tuning process of TVB-simulated models. Cobrawap is an open-source Python-based modular analysis workflow that generates standardized quantitative descriptions of brain wave phenomena, so far used for heterogeneous murine datasets of both experimental (Gutzen et al., 2024) and simulated (Capone et al., 2023) origin. Cobrawap potential for extension and embracement of a larger variety of use-cases – among which, notably, the analysis of human data – resides at its core in modularity: it consists of a series of workflow components implemented as scripts, each representing an elementary analysis or visualization operation; these *blocks* are then organized into a series of sequential *stages*, the selection and execution order of blocks in each stage being suitably configurable to fit the requirements of the input data and the analysis goal.

In this work we lay the foundations for the inter-operability of TVB and Cobrawap, acting on single blocks and on the Cobrawap structure itself, aimed at having the complete calibration and the validation of TVB-simulated models as an integrated use-case. Intrinsically, Cobrawap operates on matrices, reflecting the regular organization of sensors: each matrix element represents a *channel* associated to the spatial position corresponding to an elementary source of experimental or simulated activity – e.g. a camera pixel or an electrode – sampled at discrete points in time. To map TVB output to the Cobrawap framework, the individual neural mass of a particular node in the model is hence associated to a channel. In more detail, the 3D spatial arrangement of the N connectome nodes is re-organized into a 1D vector containing the same number of channels, arranged following the connectome

ordering (Hagmann et al., 2008). This simplified computational solution is sufficient for our analysis, since the focus is on node cross-correlations, for which only the distance among nodes in the connectome is relevant, together with TVB-encoded temporal delays.

New processing and visualization blocks have been designed for this specific TVB-tuning use-case (see following section), improving and expanding what already available within the latest Cobrawap release (Gutzen et al., 2025b); these new features are currently implemented in a dedicated development software branch, and will be implemented for full integration in the official Cobrawap software release 0.3.0.

2.5. Metrics utilized for data analysis

The following metrics were employed to comprehensively analyze the dynamics of simulated brain activity across both spontaneous and evoked conditions in the TUN and DEF configurations, unless otherwise specified.

2.5.1. Events

To characterize the node dynamics at the channel level, we identify the timestamps of transitions from low to high levels of activity in the signal evolution. In the following, we will refer to such transitions as *events*. Events were detected for each node by applying a threshold to the phase signal derived as the angle of the complex-valued analytic signal of the node (obtained via a Hilbert transform operation). In this study, a threshold of $-\pi/2$ was chosen, corresponding to the start of the upstroke. To ensure robustness, the algorithm selected only the time points where the threshold was crossed in an upward direction (from smaller to larger values), reaching a clearly identifiable peak (phase $= 0$) before the next threshold downward crossing. We obtained the average event rate by counting the total number of events during the simulation divided by the time length of the simulation itself. Additionally, we defined the time interval between events as *inter-event-time* (IET), and calculated the coefficient of variation ($\mathrm{CV_{IET}}$) of the IETs as the standard deviation of IETs divided by the mean of IETs.

2.5.2. Power Spectral Density Analysis

According to the cortical organization principles resumed in Larkum (2013), superficial layers of the cortex are reached mainly by projections from non-specific thalamic nuclei and association fibers, and the synapses established with pyramidal neurons through these paths are in majority of NMDA type. $Q_{V,network}$ and Q_V excitatory contributions in Eq. (1a) are not endowed with the slow injection times of NMDA synapses. To create a better proxy for the EEG signal and investigate it in the frequency domain, we convolved V with a bi-exponential kernel aimed to mimic synaptic currents. Also, this approach enables direct compatibility with the output of TVB simulations representing the average membrane potential of pyramidal population and not the impinging currents on that population. We selected NMDA-like parameters for emulating the synaptic activity profile in the high-activation regime (rise time constant $\tau_{rise} = 5\,\mathrm{ms}$ and decay time constant $\tau_{decay} = 20\,\mathrm{ms}$, following Gerstner et al. (2014)). Then, to obtain the synaptic activity profile of each cortical region, we averaged the convolved signal across all nodes corresponding to a given region (see Tab. A.1), thus producing 66 regional synaptic activity profiles.

The Power Spectral Density (PSD) of this synaptic activity proxy was then computed using Welch method with time segments of $70\,\mathrm{s}$ and a $50\,\%$ overlap.

As an additional measure, the PSD was computed on the hemispheric event data, obtained cumulating the number of events that occur at any node of each hemisphere using temporal bins of $5\,\mathrm{ms}$; this results in two aggregated signals (one per hemisphere) with a sampling resolution of $200\,\mathrm{Hz}$. To detect infra-slow frequencies, Welch method was applied with time segments of $140\,\mathrm{s}$ and a $50\,\%$ overlap. On the resulting PSDs, the $1/f$ background component was estimated by fitting a linear function in log-log space to obtain the PSD slope, following the method outlined in Colombo et al. (2019).

2.5.3. Time-frequency Analysis

Time-frequency decomposition was performed using a continuous wavelet transform with complex Morlet wavelets, implemented via the PyWavelets package (Lee et al., 2019). In the resting state, scales (i.e. the temporal span of wavelets) were computed for frequencies

around the main peak in the frequency spectrum in 1 Hz steps (8–12 Hz for TUN and 18–22 Hz for DEF configurations); for the evoked activity, scales ranged instead within 8–100 Hz, still in 1 Hz steps, to account for a potentially wider evoked spectrum. Each wavelet was parameterized with a normalized bandwidth of 1 and a normalized center frequency of 1; normalization depends on the sampling frequency (1 kHz). The transformation was applied using a Fast Fourier Transform (FFT)-based method, yielding complex wavelet coefficients.

The time-frequency power representation was then obtained as the squared magnitude of the complex coefficients for each frequency, then averaged over the frequency range. Only for the analysis of the evoked activity, power was also averaged across all trials, to obtain the temporal evolution of broadband post-stimulus power. To account for baseline variability, trial-averaged power time-course $\mathcal{P}$ was normalized using a decibel (dB) transformation with respect to the pre-stimulus mean:

$$\widetilde{\mathcal{P}} \equiv 10 \log_{10} \left(\mathcal{P}_{\text{post}} / \langle \mathcal{P}_{\text{pre}} \rangle \right), \tag{5}$$

where $\mathcal{P}_{\text{post}}$ represents the post-stimulus power at each time point, while $\langle \mathcal{P}_{\text{pre}} \rangle$ is the time average from -350 ms to -50 ms with respect to the stimulus onset.

To assess long-range temporal correlations in resting-state neural dynamics, we applied Detrended Fluctuation Analysis (DFA) to the amplitude envelope from wavelet transform (i.e. the frequency-average of complex coefficients magnitude). DFA quantifies long-range temporal correlations – a hallmark of critical dynamics (Linkenkaer-Hansen et al., 2001) – by measuring how fluctuations persist over increasing window sizes. We used the implementation provided in the neurodsp package (Cole et al., 2019), which first detrends the signal by removing its mean and computes the cumulative sum. The resulting signal is then divided into equal-sized windows, and within each, a linear trend is fitted. The fluctuation is computed as the mean squared deviation from this trend, and the procedure is repeated over multiple window sizes to estimate the scaling exponent. In our analysis, we used 50 window sizes, logarithmically spaced between 0.5 and 100 seconds.

2.5.4. Correlation Functions

The auto-correlation function was used to evaluate the temporal correlation of a signal with itself across varying time lags. In this study, we applied it to channel signals from both TUN and DEF configurations, considering lags up to $120\,\text{ms}$. The analysis focused on identifying the largest auto-correlation peak at lags $\neq 0$, and the corresponding *optimal* value of the lag was recorded for further analysis. Analogously, the cross-correlation function was employed to quantify the similarity between signals originating from different brain nodes across varying time lags, up to $120\,\text{ms}$ also in this case. This analysis allowed us to extract two key measures for each pair of nodes: functional connectivity $\mathbb{FC}$, defined as the peak value of the cross-correlation function, and functional lag $\mathbb{FL}$, corresponding to the lag (in ms) at which the peak occurred, where the sign of the lag reflects the direction of the interaction. For each unordered pair of nodes (i, j), two sets of $\mathbb{FC}$ and $\mathbb{FL}$ values were then computed: one where node i led node j (node i shifted back relative to j) and the other where j led i. This approach resulted in the functional connectivity matrix $\mathbb{FC}$, and the functional lag matrix $\mathbb{FL}$, which are potentially non-symmetric, thereby capturing the directionality of interactions between brain nodes.

We then quantified their asymmetry as $\mathbb{FC}_{\text{asym}} \equiv \mathbb{FC} - \mathbb{FC}^{\mathsf{T}}$ and $\mathbb{FL}_{\text{asym}} \equiv \mathbb{FL} - \mathbb{FL}^{\mathsf{T}}$, where $(\cdot)^{\mathsf{T}}$ denotes the matrix transpose. The matrix $\mathbb{FC}_{\text{asym}}$ captures directional differences in communication, with positive values $\mathbb{FC}_{\text{asym},ij} > 0$ indicating that node i exerts a stronger influence on node j than vice versa, and negative values $\mathbb{FC}_{\text{asym},ij} < 0$ indicating the opposite.

To derive a nodal asymmetry score, we finally computed the sum of asymmetry values across each row of $\mathbb{FC}_{\text{asym}}$, thus projecting into 1D the 2D representation of the matrix, and yielding a single asymmetry score per node:

$$\mathbb{A}_{\text{i}} = \sum_{j} \mathbb{FC}_{\text{asym},ij} \,, \tag{6}$$

where $\mathbb{A}_i$ represents the net asymmetry of node i, with positive values indicating a global leading role (*parent*) in the network, and negative values indicating nodes behaving as "followers" (*children*).

2.5.5. Complexity Metrics: PCI and functional complexity

The *Perturbational Complexity Index* (PCI), originally introduced by Casali et al. (2013), provides a quantitative measure of the inherent complexity of spatio-temporal EEG activity patterns evoked by Transcranial Magnetic Stimulation (TMS). In this study, we adopted a similar framework, leveraging evoked whole-brain activity simulated using TVB as a proxy of the signal reconstructed at the "sources".

To identify the significant spatio-temporal patterns of stimulus-evoked responses, we applied the non-parametric bootstrap-based statistical analysis of Casali et al. (2013) on the voltage signal of each node. The procedure, also known as maximal statistic (Nichols and Holmes, 2001), consisted of several steps. First, the evoked activity was rescaled with respect to the pre-stimuls baseline by subtracting the mean and dividing by the standard deviation of the pre-stimulus period. Second, for each node, pre-stimulus activities were randomly sampled with replacement (*bootstrapped*) from the original distribution across trials and pre-stimulus time samples. Third, for each node and time point, the mean across trials of the bootstrapped values were computed (*Jboot*). Fourth, for each pre-stimulus time point, the maximum absolute value of Jboot across nodes was obtained. This process (steps 2, 3 and 4) was repeated 500 times to build a null distribution from which the $(1 - \alpha)$ percentile was used to define a significance threshold (we used $\alpha = 0.05$). Finally, a binary spatio-temporal mask was obtained by marking samples exceeding this threshold as significant, as in Casali et al. (2013). Eventually, PCI was computed by quantifying the Lempel-Ziv complexity (Lempel and Ziv, 1976) of the binarized matrix representing significant activations, then normalized by the source entropy.

In addition, in order to asses the richness of interactions within functional connectivity matrix $\mathbb{FC}$, *functional complexity* can be computed, which quantifies the balance between functional integration and functional segregation (Zamora-López et al., 2016). A low functional complexity is characterized by narrow distributions of values in the matrix, indicating either near-total statistical independence ($\langle \mathbb{FC} \rangle \approx 0$, i.e. total functional segregation) or global synchrony ($\langle \mathbb{FC} \rangle \approx 1$, i.e. total functional integration). In contrast, complex interactions arise when the collective activity is characterized by intermediate states yielding to a

broad distribution of the $\mathbb{FC}$ values. Following this methodology, functional complexity was computed as the sum of the absolute differences over the m bins between the distribution of $\mathbb{FC}$ values and the uniform distribution over the same range, as described in Zamora-López et al. (2016).

2.5.6. Statistical Metrics

Standard statistical metrics were employed in this study, including the standard deviation (SD), representing the dispersion around the mean, and the inter-quartile range (IQR), describing the spread of the middle 50 % of the data. The coefficient of variation (CV) was used to assess relative variability (defined as the ratio of the standard deviation to the mean) and the median was used as a robust measure of central tendency.

3. Results

Building on the Larter-Breakspear model implemented in a whole-brain network via TVB, we used Cobrawap to process the TVB output and explore the differences between the tuned (TUN) configuration and the default (DEF) configuration.

3.1. Characterizing Spontaneous Dynamics: Divergent Temporal and Spectral Patterns in Tuned vs. Default Configurations

To start with, we examined the membrane potential traces recorded in the resting-state condition, shown for three representative nodes (picked from FUS, PREC, and RMF region of the right hemisphere, respectively; see Tab. A.1) in TUN (Fig. 2A) and DEF (Fig. 2C) configurations; the corresponding amplitude distributions are shown in Figs. 2B and 2D, respectively. Qualitatively, the TUN configuration exhibited more diverse activity patterns, with some nodes also displaying bursting dynamics (e.g., middle trace in Fig. 2A).

To identify the events of our interest, i.e. changes in the neural activity, we analyzed the Hilbert phase of the membrane potential and applied a threshold of $-\pi/2$, following the methodology outlined by Gutzen et al. (2024) (see Sec. 2.5.1). Figs. 2E and 2G show the rasterplots of upgoing events for the two configurations, whereas Figs. 2F and 2H illustrate

17

the histograms of the average event rate across nodes (see Sec. 2.5.1); cyan and orange bars on the left side of the two rastergrams identify nodes belonging to the two hemispheres (left and right, respectively). The same color coding is used in the bottom part of Figs. 2E and 2G, where cyan and orange traces represent the cumulated event signal of each hemisphere (see Sec. 2.5.2). A clear distinction between the two configurations emerged in the distribution of the average event rate across nodes: TUN showed a more heterogeneous pattern, compared to DEF (mean and standard deviation across channels: 9.60 ± 7.41 Hz for TUN, 18.56 ± 0.91 Hz for DEF).
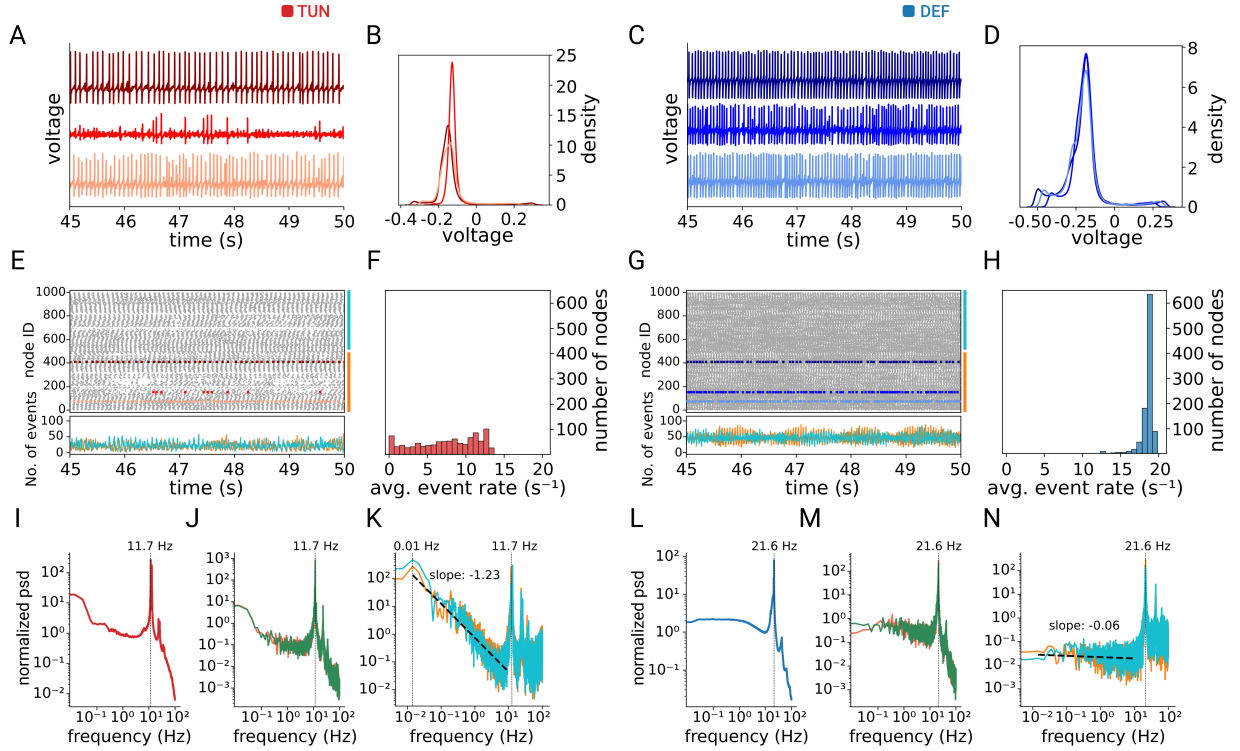
Figure 2: **Comparison of spontaneous dynamics in TUN and DEF configurations: time-domain and frequency-domain analyses.**

A) Voltage traces from three representative nodes from right-hemisphere FUS, PREC, and RMF regions (brown, red, and salmon lines, respectively) in the TUN configuration. **B)** The probability density functions of voltage distributions from nodes in A). **C-D)** Same as A) and B), respectively, for the DEF configuration. **E)** Rasterplots of upgoing transition events for each node (gray, top panel), alongside the cumulated number of detected events on the right and left hemisphere (orange and cyan, respectively, bottom panel), in the TUN configuration. Colored events in the upper panel are relative to the same sample traces shown in A).

F) Histograms of the average event rate (red filled bars) across all nodes in TUN. **G-H)** Same as E) and F), respectively, for the DEF configuration. **I)** Average PSD of synaptic activity proxy across all regions in TUN, highlighting a peak frequency at 11.7 Hz (black vertical dashed line). **J)** PSD of synaptic activity proxy of left LOCC (green line) and right LOCC (red line) in TUN, with a peak frequency at 11.7 Hz. The synaptic activity was averaged over the nodes of right and left LOCC before computing the PSD. **K)** PSD of the cumulated event signals from both hemispheres (right hemisphere: orange line; left hemisphere: cyan line), showing a low-frequency content (~ 0.01 Hz) in TUN. The black dashed oblique line represents the spectral slope, obtained by fitting a line to the average PSD in log-log space, in the frequency range 0.01–10 Hz. **L-N)** Same as I), J) and K), respectively, for the DEF configuration; notice the peak frequency at 21.6 Hz, and the absence of both the low-frequency content and the $1/f$ trend in the PSD of the cumulated event signals.

The synaptic activity proxy (see Sec. 2.5.2) was derived from the voltage traces to approximate post-synaptic currents and obtain synaptic activity profiles for each cortical region (exemplary traces shown in Fig. 1B-C). We computed both the average PSD across all cortical regions (Fig. 2I for TUN, and Fig. 2L for DEF) and the PSD for specific regions of interest (Fig. 2J for TUN, and Fig. 2M for DEF) – here, the left and right lateral occipital cortex (LOCC; see Tab. A.1). Additionally, to study the collective dynamics of the network, we computed the PSD from the cumulated event signal of the two hemispheres (Fig. 2K for TUN, and Fig. 2N for DEF; see Sec. 2.5.2), derived from the rasterplots of events. By construction of the configurations, DEF displayed a dominant frequency peak at 21.6 Hz, whereas TUN showed a peak in the alpha band at 11.7 Hz. Responsible for this shift is the change introduced on the timescale parameter t_{scale} with respect to default setting (see values in Tab. A.2 and Methods). Furthermore, TUN revealed a distinct peak at 0.01 Hz in the PSD of the cumulated event signal, absent in DEF, highlighting infra-slow network fluctuations; at odds with the dominant frequency mentioned above, this effect cannot be easily associated with the tuning of a unique parameter in the model. Notably, a $1/f$ trend was also observed in TUN (slope $= -1.23$), but was absent in DEF (slope $= -0.06$), suggesting scale-free dynamics in the former configuration only.

Overall, these findings indicate that the TUN configuration supports a richer repertoire

of dynamical activity across nodes, characterized by more heterogeneous average event rates, prominent infra-slow network fluctuations, and a scale-free $1/f$ spectral profile – hallmarks of dynamics closer to a critical regime (Chialvo, 2010; Palva and Palva, 2018).

3.2. Signal Periodicity Analysis reveals Spatially Organized Spectral Features in the Tuned Configuration

To better understand the apparent mismatch in TUN between the heterogeneous event rates across nodes (Fig. 2F) and the spectral peak at $\sim 12\,\text{Hz}$ that dominates at the global scale (Figs. 2I-K), we turned to auto-correlation analysis of the spontaneous voltage activity to capture the degree of temporal regularity of oscillations at each node. We therefore computed the auto-correlation function for each node in both TUN and DEF configurations.
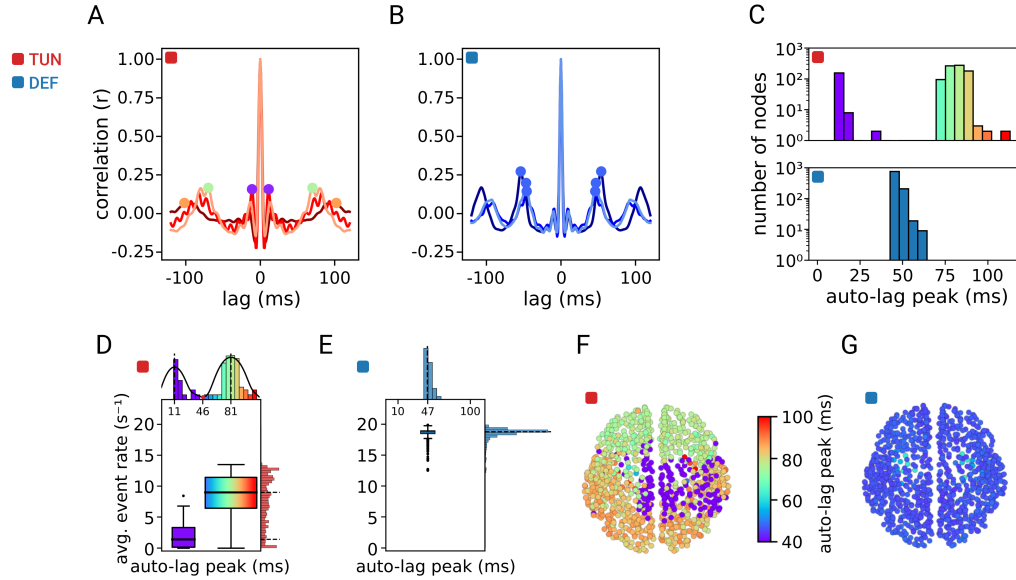

Figure 3: **Auto-correlation analysis and spatial distribution of periodicity in TUN and DEF.**
A-B) Auto-correlation functions of the spontaneous voltage signal from three representative nodes (same as in Fig. 2) for TUN (red palette) and DEF (blue palette). The largest peak at lag $\neq 0$ is marked by coloured dots. **C)** Distribution of the latencies of the dominant auto-correlation peaks (lag > 0) across brain nodes, revealing a bimodal distribution in TUN (top), while DEF (bottom) exhibits a narrow distribution centered around $50\,\text{ms}$. **D)** Relationship between signal periodicity and average event rate in TUN. Boxplots depict the average event rate for nodes grouped by short ($< 46\,\text{ms}$) and long ($> 46\,\text{ms}$) auto-correlation peaks. The nodes exhibiting periodicity in the first mode (i.e. $< 46\,\text{ms}$) are $17\,\%$ of the total. The vertical and horizontal black dashed lines on the histogram mark the median of the distributions.

20

E) Same as D), but for DEF. Here nodes are considered all together, not split into subgroups according to their auto-lag peaks. **F-G)** Spatial distribution of peak latencies mapped onto brain nodes for TUN and DEF configurations. TUN displays structured clustering, with faster periodicities in medial-central regions and a gradient between frontal and posterior regions. DEF exhibits a more homogeneous distribution of periodicities across the brain.

These functions are illustrated in Figs. 3A and 3B for three different nodes (the same as in Fig. 2, from right FUS, PREC, and RMF regions). By examining the largest auto-correlation peak at lag $\neq 0$, we observed a median periodicity of 80 ms (12.5 Hz) in TUN and 47 ms (21.3 Hz) in DEF. This periodicity aligns with the PSD results in Figs. 2I and 2L, where a peak around 12 Hz was observed for TUN, and around 22 Hz for DEF.

We hence hypothesized that the median periodicity of 80 ms and 47 ms observed in TUN and DEF, respectively, was driven by the temporal arrangement of events in the two configurations. Supporting this hypothesis, the node-averaged PSD of the events (see Suppl. Fig. A.1) revealed peaks at approximately 12 Hz in TUN and 22 Hz in DEF. We interpret this as a signature of the network periodicity (as also suggested by the PSD of the hemispheric signal in Figs. 2K and 2N), which we suggest is predictably influenced by global model parameters, such as conduction velocity and global coupling, as detailed in Supplementary Material (see Suppl. Fig. A.2).

In addition to differences in the median peak, TUN exhibited also shorter peak latencies of approximately 11 ms, as shown for a node of the right PREC region in Fig. 3A (red line and purple circles).

The distribution across nodes of the latencies of the dominant auto-correlogram peaks (Fig. 3C, with lag > 0) highlighted a clear difference between the TUN (Fig. 3C, top panel) and the DEF (Fig. 3C, bottom panel) configurations. In DEF the distribution was centered around 50 ms (median $=$ 47 ms) with low variability (SD $=$ 2.15 ms), while in TUN a bimodal distribution emerged, with a larger standard deviation (SD $=$ 26.48 ms) driven by the presence of two distinct modes centered around 11 ms and 81 ms. The underlying cause for this bimodality is the relative difference in the strength of the $\sim$80 ms and $\sim$11 ms

auto-correlogram peaks, varying node by node.

Since the auto-lag at ∼80 ms was mainly driven by the model events, we hypothesized that nodes expressing a higher strength of ∼11 ms peaks are those with a low average event rate (i.e., lower number of events), reflecting sub-threshold activity typical of nodes with irregular and bursty dynamics. An example is shown in the middle trace of Fig. 2A, corresponding to the node in the right PREC region with a peak at 11 ms in Fig. 3A.

To test this, the two modes in the TUN auto-lag peak distribution have been split considering the minimum of its Kernel Density Estimate function (found at 46 ms); this allows to separate the nodes in two groups, depending on the dominant peak in the auto-correlogram. Relating the nodes of either group to their average event rate (Fig. 3D), we observed that the average event rate in TUN was lower for nodes in the group with short lags (median=1.38 Hz; mean=1.92 Hz; SD=1.93 Hz) than for nodes in the group with long lags (median=9.00 Hz; mean=8.66 Hz; SD=3.35 Hz). We repeated the same analysis for DEF in Fig. 3E: the monomodality of DEF in the distribution of the latency is reflected by an analogous monomodality in the distribution of the average event rate (median=18.78 Hz; mean=18.56 Hz; SD=0.91 Hz). In summary, we interpret these findings such that the broad distribution of events and auto-lag peaks in the TUN configuration (vertical and horizontal histograms in Fig. 3D, respectively) is due to a superposition of a regular alpha activity and a component at 11 ms, driven by the irregular, bursting activity of nodes exhibiting more sub-threshold dynamics (i.e., lower number of events). In comparison, the DEF configuration shows a stereotyped beta oscillation that dominates the lags (Fig. 3E).

To visualize the spatial organization of these differences, we mapped the peak latencies onto a brain map (Figs. 3F and 3G). TUN exhibited a more spatially organized clustering structure compared to DEF. Indeed, in TUN (Fig. 3F) nodes with peak latencies around 11 ms were clustered within central-parietal areas. Additionally, considering the second mode after 46 ms, shorter peak latencies (corresponding to faster oscillations in the auto-correlation trace) were observed in frontal compared to posterior regions (Fig. 3F), an emergent feature of the model configuration that trends in the direction of experimental findings (Rosanova et al., 2009; Frauscher et al., 2018; Capilla et al., 2022). Conversely, DEF displayed a

homogeneous spatial distribution, corresponding to more stereotypical simulated dynamics (Fig. 3G).

Together, these results demonstrate that the tuned configuration generates richer spatio-temporal dynamics characterized by *i)* a non-trivial spatial organization of the rhythms (with both frontal-posterior latency gradients and distinct central-parietal clusters showing shorter latencies and reduced average event rates), and *ii)* an enhanced overall heterogeneity – all contrasting sharply with the homogeneous, stereotyped activity patterns in the default configuration of the model.

3.3. Spatio-temporal Irregularity and Scale-Free Dynamics in the Tuned Configuration

The results presented in Fig. 3 demonstrate that the TUN configuration exhibits spectral heterogeneity which is reflected in a distinctive spatial topography of auto-correlation peak latencies. To explore how this heterogeneity manifests in the temporal domain, we next computed the coefficient of variation of the inter-event-time (CV_{IET}; see Sec. 2.5.1) across nodes. Figs. 4A and 4B show the distribution of CV_{IET} for TUN and DEF, respectively, while Figs. 4C and 4D map these values onto the brain. Once again, we observed a more pronounced heterogeneity in TUN, which was also reflected in a non-trivial spatial organization, in contrast with DEF. Specifically, TUN exhibited more irregular (i.e., higher CV_{IET} overall, particularly in central-parietal areas) and spatially heterogeneous events, while DEF showed more regular (i.e., lower CV_{IET}) and spatially homogeneous event patterns.

Building on this observation of irregularity and heterogeneity in event timing, a complementary and related aspect to consider is the temporal fluctuation of the neural signals themselves. To examine these dynamics more closely, we performed a time-frequency decomposition using Morlet wavelet convolution to extract the power time-course within the frequency band associated with events, specifically, the 8–12 Hz range for TUN and the 18–22 Hz range for DEF, corresponding to the respective dominant frequencies in their PSDs. The power time-course (see Sec. 2.5.3) of the three representative nodes in TUN and DEF are reported in Supplementary Material (Suppl. Figs. A.3A and A.3B). To quantify power fluctuations over time, we computed their coefficient of variation (CV_{power}) across nodes

23

(Figs. 4E and 4F) and mapped it onto brain maps (Figs. 4G and 4H). Also in this case, power exhibited a high temporal and spatial regularity for DEF, resulting in a more homogeneous brain map with low and quite concentrated CV_{power} values. Conversely, we observed a heterogeneous distribution for TUN, with central areas displaying high CV_{power} values, indicative of pronounced power fluctuations. Interestingly, the average PSD across nodes of the power time-courses for TUN revealed significant infra-slow fluctuations (Suppl. Fig. A.3C) – mirroring the 0.01 Hz components observed in the network-level PSD (Fig. 2K).
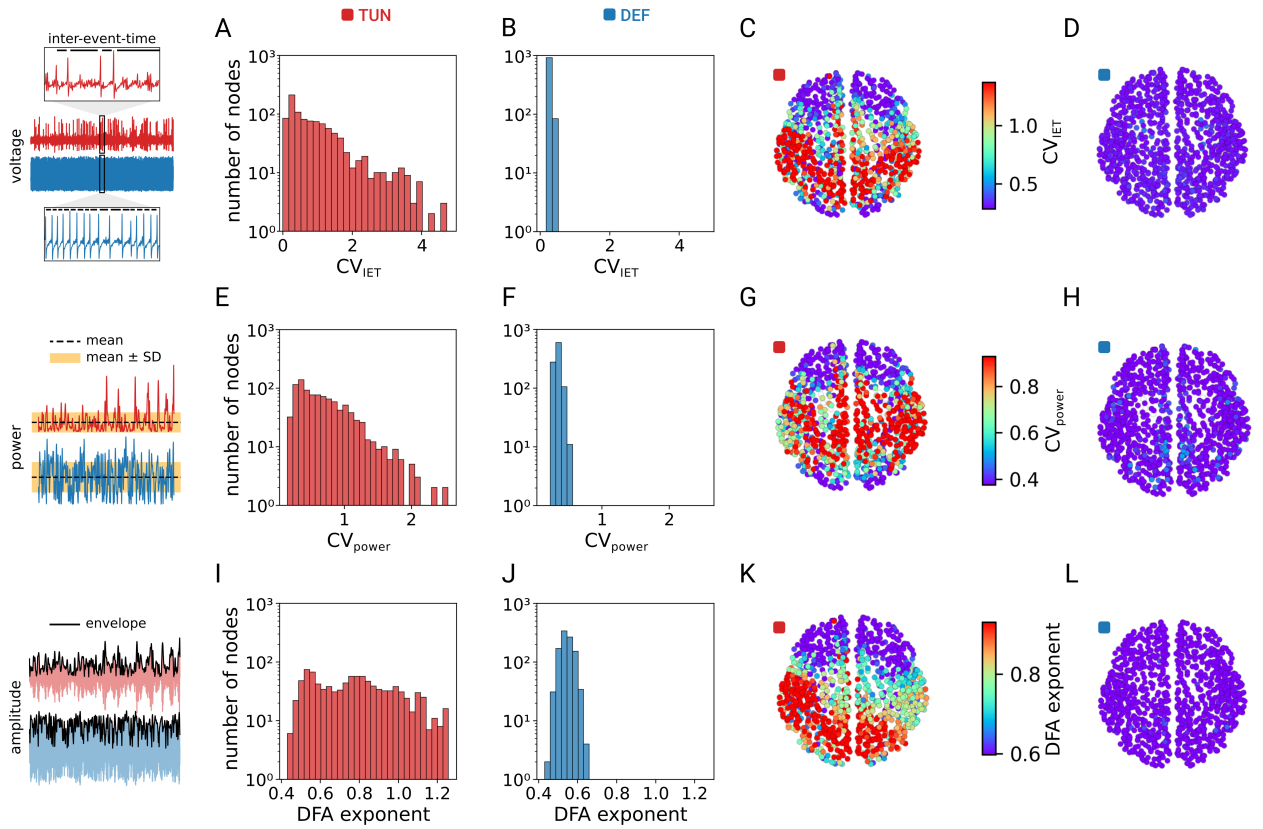

Figure 4: **Temporal and spatial variability of signal fluctuations in TUN and DEF.**
Signal processing steps are illustrated in the leftmost panels of each row: Top: Example traces show voltage fluctuations and inter-event-time (IET) used to calculate the CV_{IET}. Middle: Example power time courses used to compute the CV_{power}, with shaded regions indicating mean ± standard deviation. Bottom: Example amplitude envelope traces used to estimate the DFA exponent across nodes. **A-B)** Histograms showing the coefficient of variation of inter-event-time (CV_{IET}) across nodes for TUN and DEF configurations.

24

C-D) Spatial distribution of the CV_{IET} mapped onto brain nodes for TUN and DEF configurations. **E-F)** Histograms showing the coefficient of variation of the power time-courses (CV_{power}) across nodes, computed via Morlet wavelet convolution for TUN and DEF configurations. Power was obtained by summing within the 8–12 Hz range for TUN and the 18–22 Hz range for DEF. **G-H)** Brain maps displaying the spatial distribution of CV_{power} in TUN and DEF configurations. **I-J)** Histograms showing the DFA exponent computed for each node on the amplitude envelope in the 8–12 Hz range for TUN and the 18–22 Hz range for DEF. **K-L)** Brain maps displaying the spatial distribution of DFA exponents for TUN and DEF configurations.

This dual manifestation of infra-slow rhythms across both nodal power time-courses and network-level activity suggests a scale-free spatio-temporal organization, where infra-slow fluctuations coherently modulate the dominant alpha-band dynamics in TUN. In stark contrast, DEF exhibited a flat PSD profile for power time-courses, consistent with uncorrelated (white-noise-like) dynamics. Together with the $1/f$ scaling (Fig. 2K), these findings suggested TUN may operate near a critical regime. To test this hypothesis, we performed Detrended Fluctuation Analysis (DFA) (see Sec. 2.5.3 for details) on the 8–12 Hz (18–22 Hz for DEF) amplitude envelope. DFA exponents in TUN (Fig. 4I) spanned a broad range (exponent $\approx$ 0.5–1.2; IQR = 0.6–0.93), encompassing uncorrelated noise ($\approx$0.5), weak to strong long-range temporal correlations ($\approx$ 0.6–1.0), and persistent trends (> 1.0). This heterogeneity suggests distinct dynamical sub-populations with a specific spatial distribution (Fig. 4K): approximately 30 % of nodes fell within the range 0.8–1.0, often associated with near-critical or critical dynamics, while others exhibited either noise-like ($\approx$0.5; $\sim$16 % of nodes) or overly persistent ($>$1.0; $\sim$17 % of nodes) behavior. In contrast, DEF consistently showed noise-dominated dynamics (exponent $\sim$ 0.5–0.6) across all nodes (Figs. 4J and 4L).

3.4. Emergent Complex and Asymmetric Interactions in the Tuned Configuration

Up to this point, we have analyzed the dynamics of individual nodes, without examining their mutual interactions. To this specific aim, by leveraging cross-correlation functions one can derive two key metrics: the functional connectivity ($\mathbb{FC}$) and the functional lag ($\mathbb{FL}$) between each pair of nodes (see Sec. 2.5.4 for details). This procedure is illustrated in

Fig. 5A, where, for a given pair of nodes i and j, the cross-correlation between their time series is computed at different time lags.

The distributions of $\mathbb{FC}$ and $\mathbb{FL}$ values across all node pairs are reported in Figs. 5B and 5C. Coherently with what seen so far, TUN exhibited higher and more dispersed $\mathbb{FC}$ values than DEF, reflecting stronger and richer interactions.

It has been suggested (Zamora-López et al., 2016) that the richness of $\mathbb{FC}$ values can serve as an index of functional complexity (see Sec. 2.5.5), where the coexistence of high and low $\mathbb{FC}$ values supports a balance between functional integration (high $\mathbb{FC}$ values) and functional segregation (low $\mathbb{FC}$ values). We quantified this complexity during spontaneous activity, confirming that TUN exhibited higher functional complexity compared to DEF (inset of Fig. 5C).

The Functional Lag ($\mathbb{FL}$) (absolute values) and the Functional Connectivity($\mathbb{FC}$) matrices are displayed in Figs. 5D-E and Figs. 5G-H, respectively, alongside with the corresponding asymmetry values in Figs. 5F and 5I, derived from $\mathbb{FC}_{\text{asym}}$ (see Suppl. Fig. A.4) and $\mathbb{FL}_{\text{asym}}$ (see Sec. 2.5.4 for further details). Notably, $\mathbb{FC}$ showed a greater asymmetry in TUN, compared to DEF configuration (IQR = 0.01 for TUN; IQR = 0.006 for DEF), highlighting a prominent emergence of directional interactions in the tuned configuration. This represents a genuine emergent network phenomenon, as TUN was derived from DEF by modifying parameters in its single-node equations, without modifying the underlying connectome.

In Figs. 5J and 5K, we then quantified the asymmetry score $\mathbb{A}$ for each brain node in TUN and DEF, respectively. Starting from $\mathbb{FC}_{\text{asym}}$, we marginalized its values along each row to obtain a single asymmetry score per node (see Sec. 2.5.4 for details). Positive values indicate nodes that predominantly exert influence on others ("leading" or "parent" nodes), while negative values denote nodes that are primarily influenced by others ("following" or "child" nodes). First, we observe differences between the left and the right hemisphere, with the right hemisphere expressing more "leading" nodes. Then, mapping the asymmetry scores of the nodes to brain regions and sorting them (see Suppl. Fig. A.5), we found that the posterior cingulate cortex (PC) had the highest positive asymmetry value in both the left and right hemispheres for the TUN configuration. This result aligns with experimental

literature showing that the PC region is a primary driver of the spontaneous brain activity (Coito et al., 2018). Supplementary Fig. A.5 further highlights the differences between the left and the right hemisphere, already illustrated in Fig. 5J. Once again, DEF showed a more homogeneous behavior, with very little asymmetry values across the whole brain.
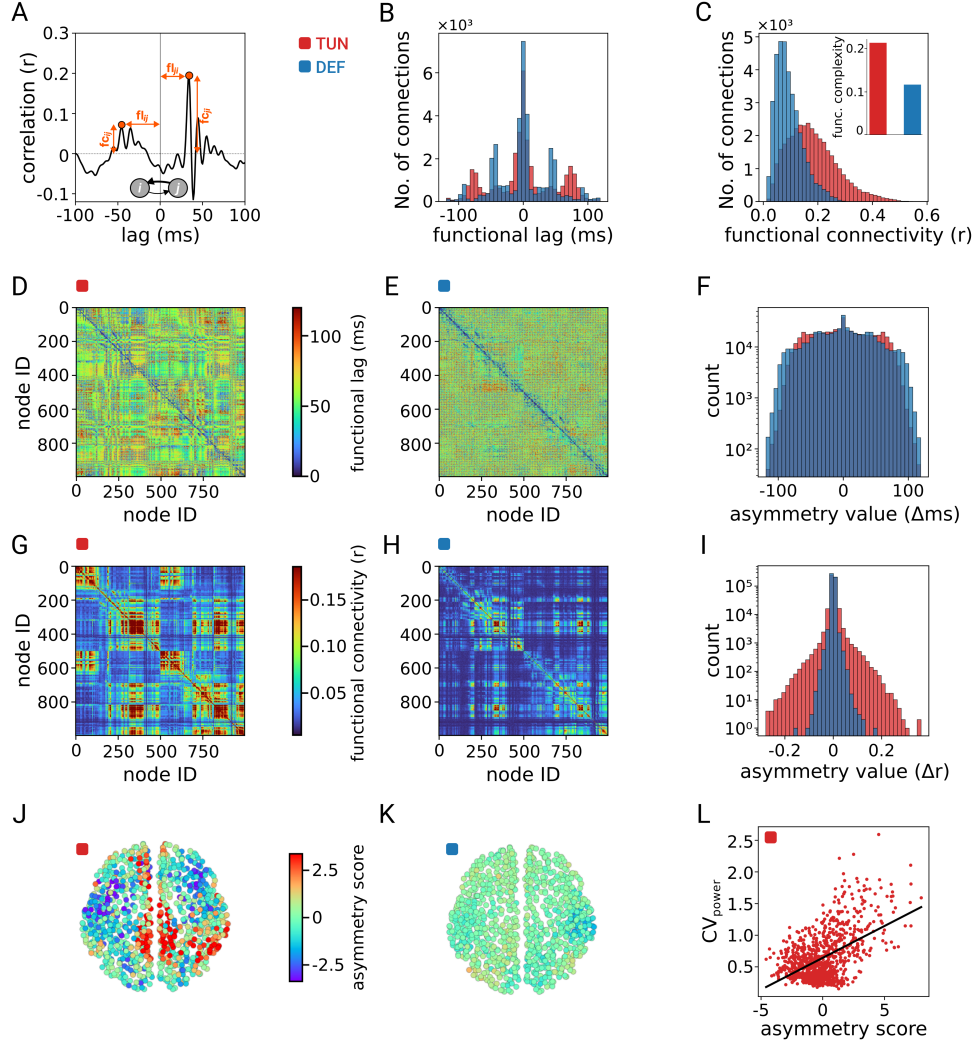

Figure 5: **Functional connectivity, functional lags, and asymmetry in TUN and DEF configurations.**

A) Illustration of the cross-correlation function applied to investigate pairwise interactions between nodes. The correlation between the time series of nodes i and j is computed at various time lags. Negative lags indicate a directional relation from i to j, while positive lags indicate the other way round. The functional connectivity ($\mathbb{FC}$) is defined as the height of the maximum correlation peak, with the corresponding lag being the functional lag ($\mathbb{FL}$). **B)** Distributions of functional lag values across all (ordered) node pairs for

the two configurations. **C)** Distributions of functional connectivity values across all (ordered) node pairs. TUN exhibits a broader $\mathbb{FC}$ distribution compared to DEF, indicating stronger and richer interactions. The inset shows the value of functional complexity. **D-E)** $\mathbb{FL}$ matrices (absolute values for the entries) for TUN and DEF configurations. **F)** Distributions of asymmetry values in $\mathbb{FL}$ matrices, derived from $\mathbb{FL}_{\mathrm{asym}}$. **G-H)** $\mathbb{FC}$ matrices for TUN and DEF configurations. **I)** Distributions of asymmetry values in $\mathbb{FC}$ matrices, derived from $\mathbb{FC}_{\mathrm{asym}}$. **J-K)** Nodal asymmetry scores $\mathbb{A}$ derived from $\mathbb{FC}$ for TUN and DEF configurations. **L)** Linear regression ($r = 0.51$, $p = 10^{-66}$) between nodal asymmetry scores $\mathbb{A}$ and $\mathrm{CV}_{\mathrm{power}}$ in TUN. Each point represents a brain node.

In Fig. 5L, eventually, we examined the relationship between the asymmetry score and power fluctuations, measured by $\mathrm{CV}_{\mathrm{power}}$. Notably, we found a significant positive correlation ($r = 0.51$, $p = 10^{-66}$), indicating that nodes with greater power variability tend to have stronger leading roles for the TUN configuration. In contrast, the same analysis for DEF revealed a non-significant relationship ($r = 0.009$, $p = 0.77$) (see Suppl. Fig. A.6).

3.5. Evoked Responses reveal Higher Spatio-temporal Complexity in the Tuned Configuration

To assess the model capacity to sustain complex stimulus-evoked dynamics, we applied 200 independent brief ($2\,\mathrm{ms}$) perturbations to the right superior parietal (rSP) nodes in both TUN and DEF configurations. The resulting evoked activity revealed striking differences between the two. In the TUN configuration, the average post-stimulus voltage exhibited richer and less stereotyped dynamics (Fig. 6A), compared to the more uniform and rapidly decaying responses observed in the DEF configuration (Fig. 6B).

To characterize the spatio-temporal profile of the evoked activity, we derived a binary spatio-temporal matrix of significant activations (see Sec. 2.5.5 for details). In TUN, significant activity was sustained over a broader temporal and spatial window (Fig. 6C), whereas in DEF it remained spatio-temporally confined to the immediate post-stimulus period and to the surroundings of the perturbed region (Fig. 6D). The prolonged perturbation effects in the TUN configuration cannot be explained solely by the reduction of the timescale parameter: while t_{scale} decreases by less than half (from 1.0 to 0.6) compared to DEF, perturbations in TUN persist nearly four times longer. The broader spatial extent of the TUN response

became especially evident when the number of significant activations was reported onto the brain maps, suggesting that in TUN the stimulus propagated far from the stimulation site, recruiting distant regions of the network (Fig. 6E). In contrast, the DEF response remained tightly localized around the stimulation site (Fig. 6F).
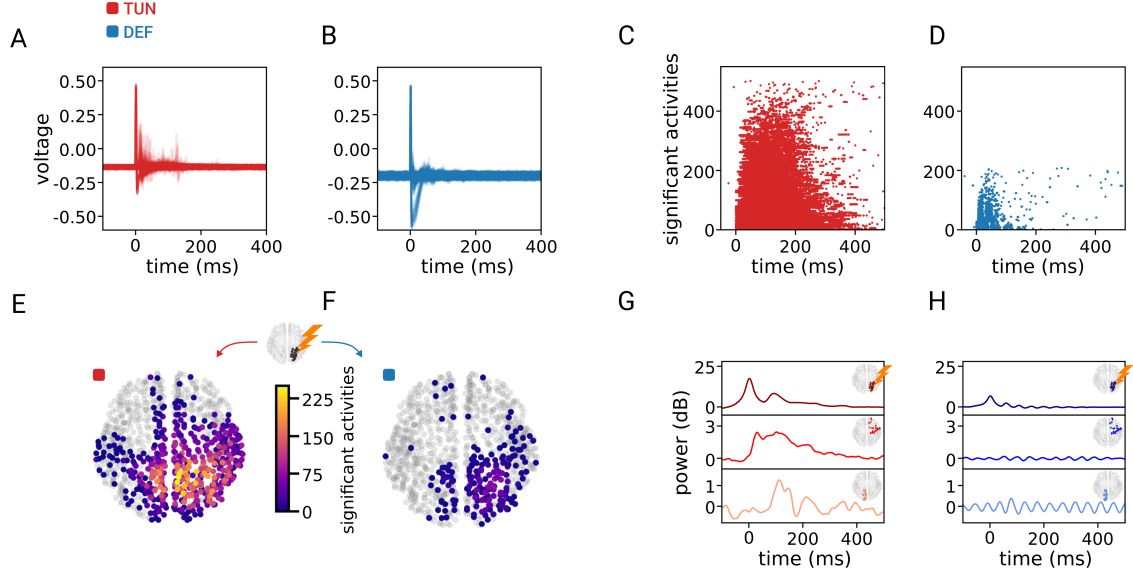

Figure 6: **Stimulus-evoked activity in TUN and DEF configurations.**
A-B) 200 independent 2 ms perturbations (i.e. 200 trials) were applied to the right superior parietal nodes (rSP) of the brain model, for both TUN and DEF configurations, to assess the spatio-temporal complexity of the evoked activity. Voltage traces averaged across trials in TUN (A, red) and DEF (B, blue) are here reported for each of the 998 nodes. **C-D)** Binary spatio-temporal matrices of significant activations across nodes (y-axis) and time (x-axis), showing more sustained and spatially distributed activity in TUN (C) relative to DEF (D), where activations are sparse and temporally constrained. **E-F)** Brain maps showing the spatial distribution of significant activations (sum over 10–500 ms post-stimulus) across nodes. The smaller brain on top of the colorbar illustrates the stimulated nodes located on the rSP cortex. In TUN (E), the stimulus spreads across distant cortical areas, while in DEF (F), the activity remains localized around the stimulation site. **G-H)** Post-stimulus broadband power (dB) averaged across three equal-sized node subsets (27 nodes): directly stimulated nodes (top), nearby connected but non-stimulated nodes (middle), and distant connected nodes (bottom). Insets indicate node locations. TUN (G) displays higher power and greater temporal variability than DEF (H), where responses are weaker and more stereotyped.

To further explore the spread and heterogeneity of the evoked activity, we computed the

post-stimulus broadband power (see Sec. 2.5.3) in three equal-sized node subsets: the directly stimulated nodes; a set of spatially nearby but non-stimulated nodes within the same hemisphere; and the most distant nodes connected to the stimulation site, as determined by structural connectivity (i.e., tract lengths). In all three subsets, the TUN configuration exhibited higher power overall, as well as greater variability in its temporal dynamics compared to the DEF configuration (Figs. 6G vs 6H).

Finally, we quantified the overall complexity of the evoked spatio-temporal patterns using the Perturbational Complexity Index (PCI; see Sec. 2.5.5). The TUN configuration reached a PCI value of 0.54, substantially higher than the 0.39 observed for DEF, confirming its ability to sustain richer, more spatially distributed and temporally diverse patterns of activity in response to brief perturbations.

4. Discussion

This study grounds on two fundamental questions: *i)* How can a brain network model be tuned to simultaneously reproduce key characteristics of both spontaneous and externally evoked neural activity? *ii)* How can we systematically evaluate the model consistency with expectations from biology and ultimately with empirical data? This work contributes to answering these questions by defining physiologically relevant metrics that are useful in guiding the exploration of model parameters, thus setting up a convenient starting point for the calibration process. The approach is iterative, where discrepancies between features exhibited by the model and biological datasets provide valuable feedback that helps refine the model parameters and improve its accuracy in reproducing the neural dynamics. These metrics could be applied equally to modeled and experimentally obtained data to yield directly comparable results, thereby strengthening the robustness of the model and exploring the boundaries of its applicability. Additionally, to enhance the reproducibility and facilitate cross-study comparisons, these metrics should be accessible to the broader neuroscience community and generalizable to accommodate diverse experimental contexts.

To achieve this, we leveraged TVB, a versatile software framework that enables the simulation of large-scale brain network models. In this study, we utilized TVB to simulate

whole-brain dynamics in both spontaneous and evoked conditions, exploring how different configurations of the same model shape the emergent neural activity. However, extracting meaningful insights from these simulations and quantitatively comparing them to empirical findings requires dedicated tools for their processing and analysis, and then back to the model for its calibration. Here, we used Cobrawap to process the TVB simulation output, which enabled us to tune model parameters, aiming at matching expectations from empirical neurophysiological patterns. This approach allowed us to make meaningful comparisons between the default TVB configuration of the model and its tuned counterpart. Cobrawap capabilities for monitoring, analyzing, and visualizing dynamic variables were instrumental in ensuring that the eventually selected network model configuration captured both spontaneous and evoked brain activity. Finally, the approach we followed proved to be essential not only for guiding the tuning process, but also for revealing significant differences between the two model configurations, thus allowing for a deeper understanding of the model itself. Notably, both TVB and Cobrawap are delivered to the EBRAINS community as *tools* of the EBRAINS Software Distribution (ESD) (EBRAINS ESD, 2025). Therefore, representing a showcase of their integration, this work is also a proof of concept towards the construction of integrated workflows in EBRAINS.

In the following, we summarize the main outcomes obtained in this work, and we drive to conclusions complementing their interpretation with findings and results from literature. First, tuning was performed such that an alpha band peak could be observed, consistent with empirical evidence highlighting the prominence of alpha rhythms during resting-state brain activity (Klimesch, 1999). This effect resulted from tuning the global time scale of the model dynamics, while at variance alpha oscillations were absent in the default model.

Second, the tuning also significantly influenced both the spectral and spatial organization of brain activity. The analysis of the temporal fluctuation of transition events from the baseline to a higher activity regime and power spectral content revealed a clear spatial organization in the tuned configuration, characterized by marked heterogeneity – a feature consistent with more realistic brain dynamics (Zhang et al., 2025). In contrast, the default configuration exhibited more homogeneous and stereotyped dynamics, with reduced

spatio-temporal variability in both events and power. Notably, these differences stem from modifications to the model equation parameters, as both configurations are based on the same underlying connectome, apart from the global coupling strength and conduction velocities.

Mapping the auto-correlation peak latencies onto the brain regions further highlighted the non-trivial spatial organization of the tuned model, where faster periodicities were observed in frontal regions, whereas slower oscillations were present in posterior regions. This spatio-temporal gradient is consistent with experimental observations (Rosanova et al., 2009; Frauscher et al., 2018; Capilla et al., 2022). Interestingly, also centro-parietal regions exhibited auto-correlation peak latencies shorter than the median periodicity of other cortical regions, thus forming a distinct cluster of cortical nodes. These populations also displayed lower average event rates, indicating fewer periods of neural mass synchronization. This pattern corresponded to more differentiated and fluctuating dynamics, as reflected by the increased variability in their power time-course.

Furthermore, our study examined the communication between nodes using cross-correlation functions. We extracted two relevant metrics to analyze nodal interactions: functional connectivity ($\mathbb{FC}$) and functional lag ($\mathbb{FL}$). Our analysis revealed that the tuned configuration of the model exhibited a wider distribution of functional connectivity ($\mathbb{FC}$) compared to the default one, suggesting a greater diversity of interactions in the former. This reflects a characteristic of complex brain dynamics that maintains a balance between integration and segregation across the network (Zhao et al., 2010; Zamora-López et al., 2016).

The emergence of a greater $\mathbb{FC}$ asymmetry in the tuned configuration is another key finding. We found more directional interactions in the tuned model with respect to the default behavior, underscoring the effect of parameter tuning in promoting asymmetric network dynamics. In turn, this could indicate the presence of emergent network motifs that are crucial for sustaining complex neuronal patterns (Coito et al., 2018; Monma et al., 2025). Notably, centro-parietal regions with higher asymmetry scores also exhibited greater power fluctuations, as reflected by a significant correlation between asymmetry scores and the CV_{power}. This finding suggests that nodes with stronger leading roles in the network exhibit

more variable neural activity, potentially enhancing their ability to coordinate information propagation, thus acting as *hubs*. Such variability may drive neuronal cascades – transient bursts of activity that could shape communication across large-scale brain networks (Rabuffo et al., 2021; Fousek et al., 2024). Notably, this asymmetry was particularly pronounced in the posterior cingulate cortex, consistent with prior experimental work (Coito et al., 2018).

Also, we observed the emergence of infra-slow rhythms ($\sim 0.01\,\mathrm{Hz}$) in the tuned configuration. These infra-slow fluctuations have been well-documented experimentally (Palva and Palva, 2012; Gutierrez-Barragan et al., 2019). A particularly interesting question arising from these findings is whether the observed spatial heterogeneity in terms of temporal variability influences these infra-slow fluctuations. Specifically, it remains unclear whether centro-parietal regions, already identified as potential hubs because of their high temporal variability and stronger leading role, act as "orchestrators" of these network infra-slow rhythms, or whether they act as "gates" that facilitate the propagation of fronto-posterior (or postero-frontal) waves across the network. This question, which we intend to explore in future research, offers a promising direction for investigating how specific regions interact with infra-slow dynamics and contribute to the reconfiguration of brain states within large-scale networks (Rabuffo et al., 2021).

Crucially, the results on spontaneous activity were also accompanied by evidence that properly tuning the model parameters can generate complex, stimulus-evoked dynamics. In line with empirical studies of brain activity (Casali et al., 2013; Sarasso et al., 2014), we found that the model was able to sustain complex spatio-temporal patterns of activation in response to external perturbations, quantified with PCI. Notably, in this work we reduced the stimulus duration from $5\,\mathrm{ms}$ to $2\,\mathrm{ms}$ – compared to the protocol used in Gaglioti et al. (2024) – to better match experimental conditions, including both intra- and extra-cranial stimulations (Comolatti et al., 2025). Despite the shorter stimulus, the model still exhibited a realistic complex response, further corroborating its ability to capture essential features of neural dynamics beyond spontaneous fluctuations.

An integrative framework linking our spontaneous and evoked dynamics results is provided by criticality – a dynamical regime emerging near phase transitions, where systems

exhibit a unique balance between ordered and disordered activity (Beggs and Plenz, 2003; Chialvo, 2010; O'Byrne and Jerbi, 2022). In this regime, scale-free properties naturally arise, including $1/f$ spectral scaling (He et al., 2010), long-range temporal correlations (Linkenkaer-Hansen et al., 2001), and activity fluctuations across spatio-temporal scales, such as infra-slow fluctuations (Palva and Palva, 2012, 2018) along with heightened sensitivity to external perturbations (O'Byrne and Jerbi, 2022), which collectively maximize information capacity (Shew and Plenz, 2012). In the tuned configuration, such signatures emerged naturally: $1/f$ spectra, infra-slow fluctuations, scale-free DFA exponents, and spatio-temporal variability in both spontaneous and evoked activity. Notably, the heightened sensitivity to brief stimuli (2 ms) in the tuned configuration – manifested as prolonged, complex responses – resembles the amplified perturbation effects seen in critical systems. The prolonged perturbation effect suggests the "critical slowing down" characteristic of systems near critical points (Meisel et al., 2015), with longer relaxation timescales, while the richness of spatio-temporal patterns measured with PCI suggests efficient signal propagation through the network. Together with empirical links between PCI and criticality (Maschke et al., 2024), these results suggest that parameter tuning shifted the model toward a critical-like regime, closer to the dynamical richness of biological systems.

4.1. Limitations and future directions

While our study demonstrated how to tune models to capture macroscopic features of brain dynamics, it is important to acknowledge some limitations. First, we focused on reproducing expected large-scale characteristics of neural activity without directly comparing the model output to empirical data. However, our approach lays the foundation for such quantitative calibration by implementing a set of metrics designed to assess experimental features and applying them to the model. These metrics not only aid in the proper calibration process but also provide a framework for exploring dependencies among observables. If an emergent pattern is confirmed or refuted by experimental data, it raises important questions regarding its relationship with the initial model assumptions: Are these observables independent? Do they share a causal link? Or is their relationship mediated by additional

34

factors? Addressing these questions could offer novel perspectives for data analysis and contribute to a deeper understanding of the underlying neural mechanisms.

Second, the model itself remains a simplified representation of cortical dynamics. The neural masses used in our simulations rely on coarse-grained equations that phenomenologically describe synchronization processes at a population level, without explicitly modeling the finer-scale biophysical mechanisms that underlie neural activity. Additionally, our model does not include subcortical structures, which are known to play a fundamental role in orchestrating brain rhythms and propagating neural activity. Incorporating these structures in future work will allow us to investigate how the observed phenomena change when subcortical dynamics and their interactions with the cortex are considered.

Finally, our analysis primarily focused on a stationary characterization of the model dynamics, identifying fixed patterns of spontaneous activity. However, the brain does not operate in a steady state – it exhibits transient dynamics, shifting between different functional configurations over time. Future studies will aim to extend this work by exploring the temporal evolution of network states, classifying these transient states, and ultimately comparing them with empirical data. This will further improve model calibration and help refine our understanding of how large-scale neural networks reconfigure over time.

4.2. Conclusion

In summary, this study demonstrated the importance of parameter tuning in capturing the full complexity of spontaneous and evoked brain dynamics. The use of Cobrawap was instrumental in refining the model and ensuring its consistency with empirical expectations, allowing us to reproduce key brain activity features such as alpha-band oscillations, infra-slow rhythms, spatio-temporal heterogeneity in network activity and complex evoked responses. Our findings establish a proof of concept for a methodology that bridges computational simulations and experimental data in humans, laying the groundwork for future quantitative applications of this approach aimed at the calibration and validation of accurate and reliable whole-brain models.

We introduced a set of metrics that are made available as an independent component,

not biased by the choice of a specific simulation engine. The metrics, here employed to support the tuning process, can also be used for the cross-comparisons between simulators, and the direct comparisons with experimental data.

This opens the possibility of integrating computational and empirical approaches more systematically, leveraging automated tools such as the Learning-to-Learn (L2L) framework (Yegenoglu et al., 2022) to refine model parameters in a data-driven manner. By providing a structured approach to comparing simulated and experimental neural activity, our work highlights a pathway toward more robust, interpretable, and generalizable models of brain function.

More broadly, these results emphasize the necessity of using appropriate calibration strategies and quantitative metrics to enhance the realism and predictive power of computational models. Moving forward, this approach could facilitate the systematic investigation of how spatial variability and infra-slow rhythms shape brain network behavior, offering new perspectives on the mechanisms underlying brain state repertoires.

CRediT authorship contribution statement

Gianluca Gaglioti: Conceptualization, Formal analysis, Investigation, Methodology, Software, Visualization, Writing - Original Draft, Writing - Review & Editing. **Alessandra Cardinale:** Formal analysis, Methodology, Software, Visualization, Writing - original draft, Writing - review & editing. **Cosimo Lupo:** Conceptualization, Formal analysis, Investigation, Methodology, Software, Supervision, Writing - original draft, Writing - review & editing. **Thierry Nieus:** Conceptualization, Formal analysis, Investigation, Methodology, Supervision, Writing - original draft, Writing - review & editing. **Federico Marmoreo:** Methodology, Software, Writing - review & editing. **Robin Gutzen:** Methodology, Software, Writing - review & editing. **Michael Denker:** Methodology, Software, Writing - review & editing. **Andrea Pigorini:** Conceptualization, Project administration, Writing - review & editing. **Marcello Massimini:** Conceptualization, Funding acquisition, Project administration, Supervision, Writing - review & editing. **Pier Stanislao Paolucci:** Conceptualization, Formal analysis, Funding acquisition, Investigation, Methodology, Project

administration, Supervision, Writing - original draft, Writing - review & editing. **Simone Sarasso:** Conceptualization, Funding acquisition, Supervision, Writing - review & editing. **Giulia De Bonis:** Conceptualization, Formal analysis, Investigation, Methodology, Software, Supervision, Writing - original draft, Writing - review & editing.

Data availability

Whole-brain simulations relied on software release 2.7.2 of TheVirtualBrain (TVB) (`https://www.thevirtualbrain.org/tvb/zwei/brainsimulator-software`), with parameters as in Tab. A.2. Simulation outputs have then been analyzed with dedicated tools; their integration in the next official Cobrawap software release 0.3.0 is currently underway (the latest stable release is always reachable at `https://doi.org/10.5281/zenodo.10198748`), though new software features developed for this paper are already available as a development branch at `https://github.com/APE-group/cobrawap/tree/devs/TVB`. The code for reproducing the figures present in this plot is available upon request.

Fundings

References

Alstott, J., Breakspear, M., Hagmann, P., Cammoun, L., Sporns, O., 2009. Modeling the Impact of Lesions in the Human Brain. PLOS Computational Biology 5, e1000408. doi:10.1371/journal.pcbi.1000408.

Beggs, J.M., Plenz, D., 2003. Neuronal avalanches in neocortical circuits. The Journal of Neuroscience 23, 11167–11177. doi:10.1523/jneurosci.23-35-11167.2003.

Berger, H., 1929. Über das Elektrenkephalogramm des Menschen. Archiv für Psychiatrie und Nervenkrankheiten 87, 527–570. doi:10.1007/BF01797193.

Breakspear, M., 2017. Dynamic models of large-scale brain activity. Nature Neuroscience 20, 340–352. doi:10.1038/nn.4497.

Breakspear, M., Stam, C.J., 2005. Dynamics of a neural system with a multiscale architecture. Philosophical Transactions of the Royal Society B: Biological Sciences 360, 1051–1074. doi:10.1098/rstb.2005.1643.

Breakspear, M., Terry, J.R., 2002. Nonlinear interdependence in neural systems: motivation, theory, and relevance. The International Journal of Neuroscience 112, 1263–1284. doi:10.1080/00207450290026193.

Breakspear, M., Terry, J.R., Friston, K.J., 2003. Modulation of excitatory synaptic coupling facilitates synchronization and complex dynamics in a biophysical model of neuronal dynamics. Network (Bristol, England) 14, 703–732.

Cakan, C., Jajcay, N., Obermayer, K., 2023. neurolib: A Simulation Framework for Whole-Brain Neural Mass Modeling. Cognitive Computation 15, 1132–1152. doi:10.1007/s12559-021-09931-9.

Capilla, A., Arana, L., García-Huéscar, M., Melcón, M., Gross, J., Campo, P., 2022. The natural frequencies of the resting human brain: An MEG-based atlas. NeuroImage 258, 119373. doi:10.1016/j.neuroimage.2022.119373.

Capone, C., De Luca, C., De Bonis, G., Gutzen, R., Bernava, I., Pastorelli, E., Simula, F., Lupo, C., Tonielli, L., Resta, F., Allegra Mascaro, A.L., Pavone, F., Denker, M., Paolucci, P.S., 2023. Simulations approaching data: cortical slow waves in inferred models of the whole hemisphere of mouse. Communications Biology 6, 1–14. doi:10.1038/s42003-023-04580-0.

Casali, A.G., Gosseries, O., Rosanova, M., Boly, M., Sarasso, S., Casali, K.R., Casarotto, S., Bruno, M.A., Laureys, S., Tononi, G., Massimini, M., 2013. A Theoretically Based Index of Consciousness Independent of Sensory Processing and Behavior. Science Translational Medicine 5, 198ra105–198ra105. doi:10.1126/scitranslmed.3006294.

Casarotto, S., Comanducci, A., Rosanova, M., Sarasso, S., Fecchio, M., Napolitani, M., Pigorini, A., Casali, A.G., Trimarchi, P.D., Boly, M., Gosseries, O., Bodart, O., Curto, F., Landi, C., Mariotti, M., Devalle, G., Laureys, S., Tononi, G., Massimini, M., 2016. Stratification of unresponsive patients by an independently validated index of brain complexity. Annals of Neurology 80, 718–729. doi:10.1002/ana.24779.

Chialvo, D.R., 2010. Emergent complex neural dynamics. Nature Physics 6, 744–750. doi:10.1038/nphys1803.

Cocchi, L., Gollo, L.L., Zalesky, A., Breakspear, M., 2017. Criticality in the brain: A synthesis of neurobiology, models and cognition. Progress in Neurobiology 158, 132–152. doi:10.1016/j.pneurobio.2017.07.002.

Coito, A., Michel, C.M., Vulliemoz, S., Plomp, G., 2018. Directed functional connections underlying spontaneous brain activity. Human Brain Mapping 40, 879–888. doi:10.1002/hbm.24418.

Cole, S., Donoghue, T., Gao, R., Voytek, B., 2019. Neurodsp: A package for neural digital signal processing. Journal of Open Source Software 4. doi:10.21105/joss.01272.

Colombo, M.A., Napolitani, M., Boly, M., Gosseries, O., Casarotto, S., Rosanova, M., Brichant, J.F., Boveroux, P., Rex, S., Laureys, S., Massimini, M., Chieregato, A., Sarasso,

S., 2019. The spectral exponent of the resting eeg indexes the presence of consciousness during unresponsiveness induced by propofol, xenon, and ketamine. NeuroImage 189, 631–644. doi:`10.1016/j.neuroimage.2019.01.024`.

Comolatti, R., Hassan, G., Mikulan, E., Russo, S., Colombo, M.A., Litterio, E., Furregoni, G., D'Ambrosio, S., Fecchio, M., Parmigiani, S., Sartori, I., Casarotto, S., Pigorini, A., Massimini, M., 2025. Transcranial magnetic vs intracranial electric stimulation: a direct comparison of their effects via scalp eeg recordings. Brain Stimulation URL: `http://dx.doi.org/10.1016/j.brs.2025.07.016`, doi:`10.1016/j.brs.2025.07.016`.

Deco, G., Jirsa, V.K., 2012. Ongoing cortical activity at rest: Criticality, multistability, and ghost attractors. The Journal of Neuroscience 32, 3366–3375. doi:`10.1523/jneurosci.2523-11.2012`.

Deco, G., Jirsa, V.K., McIntosh, A.R., 2011. Emerging concepts for the dynamical organization of resting-state activity in the brain. Nature Reviews Neuroscience 12, 43–56. doi:`10.1038/nrn2961`.

Deco, G., Kringelbach, M.L., Jirsa, V.K., Ritter, P., 2017. The dynamics of resting fluctuations in the brain: metastability and its dynamical cortical core. Scientific Reports 7, 3095. doi:`10.1038/s41598-017-03073-5`.

Denker, M., Yegenoglu, A., Grün, S., 2018. Collaborative HPC-enabled workflows on the HBP Collaboratory using the Elephant framework, in: Neuroinformatics 2018, p. P19. URL: `https://abstracts.g-node.org/conference/NI2018/abstracts#/uuid/023bec4e-0c35-4563-81ce-2c6fac282abd`, doi:`10.12751/incf.ni2018.0019`.

EBRAINS ESD, 2025. `https://gitlab.ebrains.eu/ri/tech-hub/platform/esd`.

EBRAINS: Europe Research Infrastructure for Brain Research, 2023. `www.ebrains.eu`.

Endo, H., Hiroe, N., Yamashita, O., 2020. Evaluation of Resting Spatio-Temporal Dynamics of a Neural Mass Model Using Resting fMRI Connectivity and EEG Microstates. Frontiers in Computational Neuroscience 13.

Esteban, O., Markiewicz, C.J., Blair, R.W., Moodie, C.A., Isik, A.I., Erramuzpe, A., Kent, J.D., Goncalves, M., DuPre, E., Snyder, M., Oya, H., Ghosh, S.S., Wright, J., Durnez, J., Poldrack, R.A., Gorgolewski, K.J., 2019. fMRIPrep: a robust preprocessing pipeline for functional MRI. Nature Methods 16, 111–116. doi:10.1038/s41592-018-0235-4.

Fischl, B., 2012. FreeSurfer. NeuroImage 62, 774–781. doi:10.1016/j.neuroimage.2012.01.021.

Fousek, J., Rabuffo, G., Gudibanda, K., Sheheitli, H., Petkoski, S., Jirsa, V., 2024. Symmetry breaking organizes the brain's resting state manifold. Scientific Reports 14, 31970. doi:10.1038/s41598-024-83542-w.

Fox, M.D., Raichle, M.E., 2007. Spontaneous fluctuations in brain activity observed with functional magnetic resonance imaging. Nature Reviews Neuroscience 8, 700–711. doi:10.1038/nrn2201.

Frauscher, B., von Ellenrieder, N., Zelmann, R., Doležalová, I., Minotti, L., Olivier, A., Hall, J., Hoffmann, D., Nguyen, D.K., Kahane, P., Dubeau, F., Gotman, J., 2018. Atlas of the normal intracranial electroencephalogram: neurophysiological awake activity in different cortical areas. Brain 141, 1130–1144. doi:10.1093/brain/awy035.

Freyer, F., Aquino, K., Robinson, P.A., Ritter, P., Breakspear, M., 2009. Bistability and Non-Gaussian Fluctuations in Spontaneous Cortical Activity. Journal of Neuroscience 29, 8512–8524. doi:10.1523/JNEUROSCI.0754-09.2009.

Freyer, F., Roberts, J.A., Becker, R., Robinson, P.A., Ritter, P., Breakspear, M., 2011. Biophysical Mechanisms of Multistability in Resting-State Cortical Rhythms. Journal of Neuroscience 31, 6353–6361. doi:10.1523/JNEUROSCI.6693-10.2011.

Gaglioti, G., Nieus, T.R., Massimini, M., Sarasso, S., 2024. Investigating the Impact of Local Manipulations on Spontaneous and Evoked Brain Complexity Indices: A Large-Scale Computational Model. Applied Sciences 14, 890. doi:10.3390/app14020890.

Gerstner, W., Kistler, W.M., Naud, R., Paninski, L., 2014. Neuronal dynamics: From single neurons to networks and models of cognition. Cambridge University Press.

Gollo, L.L., Breakspear, M., 2014. The frustrated brain: from dynamics on motifs to communities and networks. Philosophical Transactions of the Royal Society B: Biological Sciences 369, 20130532. doi:`10.1098/rstb.2013.0532`.

Gollo, L.L., Zalesky, A., Hutchison, R.M., van den Heuvel, M., Breakspear, M., 2015. Dwelling quietly in the rich club: brain network determinants of slow cortical fluctuations. Philosophical Transactions of the Royal Society B: Biological Sciences 370, 20140165. doi:`10.1098/rstb.2014.0165`.

Gramfort, A., Luessi, M., Larson, E., Engemann, D.A., Strohmeier, D., Brodbeck, C., Goj, R., Jas, M., Brooks, T., Parkkonen, L., Hämäläinen, M., 2013. MEG and EEG data analysis with MNE-Python. Frontiers in Neuroscience 7, 267. doi:`10.3389/fnins.2013.00267`.

Griffiths, J.D., Bastiaens, S.P., Kaboodvand, N., 2022. Whole-Brain Modelling: Past, Present, and Future. Advances in Experimental Medicine and Biology 1359, 313–355. doi:`10.1007/978-3-030-89439-9_13`.

Gutierrez-Barragan, D., Basson, M.A., Panzeri, S., Gozzi, A., 2019. Infraslow State Fluctuations Govern Spontaneous fMRI Network Dynamics. Current Biology 29, 2295–2306.e5. doi:`10.1016/j.cub.2019.06.017`.

Gutzen, R., De Bonis, G., De Luca, C., Pastorelli, E., Capone, C., Allegra Mascaro, A.L., Resta, F., Manasanch, A., Pavone, F.S., Sanchez-Vives, M.V., Mattia, M., Grün, S., Paolucci, P.S., Denker, M., 2024. A modular and adaptable analysis pipeline to compare slow cerebral rhythms across heterogeneous datasets. Cell Reports Methods 4, 100681. doi:`10.1016/j.crmeth.2023.100681`.

Gutzen, R., Lupo, C., Marmoreo, F., De Bonis, G., De Luca, C., Pastorelli, E., Capone, C., Allegra Mascaro, A.L., Resta, F., Manasanch, A., Pavone, F.S., Sanchez-Vives, M.V.,

Mattia, M., Grün, S., Paolucci, P.S., Denker, M., 2025a. Cobrawap documentation. https://cobrawap.readthedocs.io.

Gutzen, R., Lupo, C., Marmoreo, F., De Bonis, G., De Luca, C., Pastorelli, E., Capone, C., Allegra Mascaro, A.L., Resta, F., Manasanch, A., Pavone, F.S., Sanchez-Vives, M.V., Mattia, M., Grün, S., Paolucci, P.S., Denker, M., 2025b. Cobrawap official releases on zenodo. doi:10.5281/zenodo.10198748.

Gutzen, R., von Papen, M., Trensch, G., Quaglio, P., Grün, S., Denker, M., 2018. Reproducible neural network simulations: Statistical methods for model validation on the level of network activity data. Frontiers in Neuroinformatics 12. doi:10.3389/fninf.2018.00090.

Hagmann, P., Cammoun, L., Gigandet, X., Meuli, R., Honey, C.J., Wedeen, V.J., Sporns, O., 2008. Mapping the Structural Core of Human Cerebral Cortex. PLOS Biology 6, e159. doi:10.1371/journal.pbio.0060159.

He, B.J., Zempel, J.M., Snyder, A.Z., Raichle, M.E., 2010. The temporal structures and functional significance of scale-free brain activity. Neuron 66, 353–369. doi:10.1016/j.neuron.2010.04.020.

Heitmann, S., Aburn, M.J., Breakspear, M., 2018. The Brain Dynamics Toolbox for Matlab. Neurocomputing 315, 82–88. doi:10.1016/j.neucom.2018.06.026.

van den Heuvel, M.P., Sporns, O., 2013. Network hubs in the human brain. Trends in Cognitive Sciences 17, 683–696. doi:10.1016/j.tics.2013.09.012.

Honey, C.J., Kötter, R., Breakspear, M., Sporns, O., 2007. Network structure of cerebral cortex shapes functional connectivity on multiple time scales. Proceedings of the National Academy of Sciences of the United States of America 104, 10240–10245. doi:10.1073/pnas.0701519104.

Honey, C.J., Sporns, O., 2008. Dynamical consequences of lesions in cortical networks. Human Brain Mapping 29, 802–809. doi:10.1002/hbm.20579.

Honey, C.J., Sporns, O., Cammoun, L., Gigandet, X., Thiran, J.P., Meuli, R., Hagmann, P., 2009. Predicting human resting-state functional connectivity from structural connectivity. Proceedings of the National Academy of Sciences 106, 2035–2040. doi:`10.1073/pnas.0811168106`.

Jensen, O., Mazaheri, A., 2010. Shaping Functional Architecture by Oscillatory Alpha Activity: Gating by Inhibition. Frontiers in Human Neuroscience 4. doi:`10.3389/fnhum.2010.00186`.

Klimesch, W., 1999. EEG alpha and theta oscillations reflect cognitive and memory performance: a review and analysis. Brain Research. Brain Research Reviews 29, 169–195. doi:`10.1016/s0165-0173(98)00056-3`.

Larkum, M., 2013. A cellular mechanism for cortical associations: an organizing principle for the cerebral cortex. Trends in Neurosciences 36, 141–151. doi:`10.1016/j.tins.2012.11.006`.

Larter, R., Speelman, B., Worth, R.M., 1999. A coupled ordinary differential equation lattice model for the simulation of epileptic seizures. Chaos: An Interdisciplinary Journal of Nonlinear Science 9, 795–804. doi:`10.1063/1.166453`.

Lee, G., Gommers, R., Waselewski, F., Wohlfahrt, K., O'Leary, A., 2019. PyWavelets: A Python package for wavelet analysis. Journal of Open Source Software 4, 1237. doi:`10.21105/joss.01237`.

Lempel, A., Ziv, J., 1976. On the complexity of finite sequences. IEEE Transactions on Information Theory 22, 75–81. doi:`10.1109/TIT.1976.1055501`.

Linkenkaer-Hansen, K., Nikouline, V.V., Palva, J.M., Ilmoniemi, R.J., 2001. Long-range temporal correlations and scaling behavior in human brain oscillations. The Journal of Neuroscience 21, 1370–1377. doi:`10.1523/jneurosci.21-04-01370.2001`.

Maschke, C., O'Byrne, J., Colombo, M.A., Boly, M., Gosseries, O., Laureys, S., Rosanova, M., Jerbi, K., Blain-Moraes, S., 2024. Critical dynamics in spontaneous eeg predict

anesthetic-induced loss of consciousness and perturbational complexity. Communications Biology 7. doi:`10.1038/s42003-024-06613-8`.

Meisel, C., Klaus, A., Kuehn, C., Plenz, D., 2015. Critical slowing down governs the transition to neuron spiking. PLOS Computational Biology 11, e1004097. doi:`10.1371/journal.pcbi.1004097`.

Monma, N., Yamamoto, H., Fujiwara, N., Murota, H., Moriya, S., Hirano-Iwata, A., Sato, S., 2025. Directional intermodular coupling enriches functional complexity in biological neuronal networks. Neural Networks 184, 106967. doi:`10.1016/j.neunet.2024.106967`.

Nichols, T.E., Holmes, A.P., 2001. Nonparametric permutation tests for functional neuroimaging: A primer with examples. Human Brain Mapping 15, 1–25. doi:`10.1002/hbm.1058`.

O'Byrne, J., Jerbi, K., 2022. How critical is brain criticality? Trends in Neurosciences 45, 820–837. doi:`10.1016/j.tins.2022.08.007`.

Palva, J.M., Palva, S., 2012. Infra-slow fluctuations in electrophysiological recordings, blood-oxygenation-level-dependent signals, and psychophysical time series. NeuroImage 62, 2201–2211. doi:`10.1016/j.neuroimage.2012.02.060`.

Palva, S., Palva, J.M., 2018. Roles of brain criticality and multiscale oscillations in temporal predictions for sensorimotor processing. Trends in Neurosciences 41, 729–743. doi:`10.1016/j.tins.2018.08.008`.

Rabuffo, G., Fousek, J., Bernard, C., Jirsa, V., 2021. Neuronal Cascades Shape Whole-Brain Functional Dynamics at Rest. eNeuro 8. doi:`10.1523/ENEURO.0283-21.2021`.

Roberts, J.A., Gollo, L.L., Abeysuriya, R.G., Roberts, G., Mitchell, P.B., Woolrich, M.W., Breakspear, M., 2019. Metastable brain waves. Nature Communications 10, 1056. doi:`10.1038/s41467-019-08999-0`.

Rosanova, M., Casali, A.G., Bellina, V., Resta, F., Mariotti, M., Massimini, M., 2009. Natural Frequencies of Human Corticothalamic Circuits. Journal of Neuroscience 29, 7679–7685. doi:`10.1523/JNEUROSCI.0445-09.2009`.

Rosanova, M., Gosseries, O., Casarotto, S., Boly, M., Casali, A.G., Bruno, M.A., Mariotti, M., Boveroux, P., Tononi, G., Laureys, S., Massimini, M., 2012. Recovery of cortical effective connectivity and recovery of consciousness in vegetative patients. Brain 135, 1308–1320. doi:`10.1093/brain/awr340`.

Sanz-Leon, P., Knock, S.A., Spiegler, A., Jirsa, V.K., 2015. Mathematical framework for large-scale brain network modeling in The Virtual Brain. NeuroImage 111, 385–430. doi:`10.1016/j.neuroimage.2015.01.002`.

Sanz-Leon, P., Knock, S.A., Woodman, M.M., Domide, L., Mersmann, J., McIntosh, A.R., Jirsa, V., 2013. The Virtual Brain: a simulator of primate brain network dynamics. Frontiers in Neuroinformatics 7. doi:`10.3389/fninf.2013.00010`.

Sarasso, S., Rosanova, M., Casali, A.G., Casarotto, S., Fecchio, M., Boly, M., Gosseries, O., Tononi, G., Laureys, S., Massimini, M., 2014. Quantifying cortical EEG responses to TMS in (un)consciousness. Clinical EEG and neuroscience 45, 40–49. doi:`10.1177/1550059413513723`.

Shew, W.L., Plenz, D., 2012. The functional benefits of criticality in the cortex. The Neuroscientist 19, 88–100. doi:`10.1177/1073858412445487`.

Sunkin, S.M., Ng, L., Lau, C., Dolbeare, T., Gilbert, T.L., Thompson, C.L., Hawrylycz, M., Dang, C., 2013. Allen Brain Atlas: an integrated spatio-temporal portal for exploring the central nervous system. Nucleic Acids Research 41, D996–D1008. doi:`10.1093/nar/gks1042`.

Tagliazucchi, E., von Wegner, F., Morzelewski, A., Brodbeck, V., Laufs, H., 2012. Dynamic BOLD functional connectivity in humans and its electrophysiological correlates. Frontiers in Human Neuroscience 6, 339. doi:`10.3389/fnhum.2012.00339`.

Trensch, G., Gutzen, R., Blundell, I., Denker, M., Morrison, A., 2018. Rigorous neural network simulations: A model substantiation methodology for increasing the correctness of simulation results in the absence of experimental validation data. Frontiers in Neuroinformatics 12. doi:`10.3389/fninf.2018.00081`.

Van Essen, D.C., Ugurbil, K., Auerbach, E., Barch, D., Behrens, T.E.J., Bucholz, R., Chang, A., Chen, L., Corbetta, M., Curtiss, S.W., Della Penna, S., Feinberg, D., Glasser, M.F., Harel, N., Heath, A.C., Larson-Prior, L., Marcus, D., Michalareas, G., Moeller, S., Oostenveld, R., Petersen, S.E., Prior, F., Schlaggar, B.L., Smith, S.M., Snyder, A.Z., Xu, J., Yacoub, E., WU-Minn HCP Consortium, 2012. The Human Connectome Project: a data acquisition perspective. NeuroImage 62, 2222–2231. doi:`10.1016/j.neuroimage.2012.02.018`.

Väyrynen, T., Helakari, H., Korhonen, V., Tuunanen, J., Huotari, N., Piispala, J., Kallio, M., Raitamaa, L., Kananen, J., Järvelä, M., Matias Palva, J., Kiviniemi, V., 2023. Infra-slow fluctuations in cortical potentials and respiration drive fast cortical EEG rhythms in sleeping and waking states. Clinical Neurophysiology 156, 207–219. doi:`10.1016/j.clinph.2023.10.013`.

Yegenoglu, A., Subramoney, A., Hater, T., Jimenez-Romero, C., Klijn, W., Pérez Martín, A., van der Vlag, M., Herty, M., Morrison, A., Diaz-Pier, S., 2022. Exploring Parameter and Hyper-Parameter Spaces of Neuroscience Models on High Performance Computers With Learning to Learn. Frontiers in Computational Neuroscience 16. doi:`10.3389/fncom.2022.885207`.

Zamora-López, G., Chen, Y., Deco, G., Kringelbach, M.L., Zhou, C., 2016. Functional complexity emerging from anatomical constraints in the brain: the significance of network modularity and rich-clubs. Scientific Reports 6, 38424. doi:`10.1038/srep38424`.

Zhang, J., Wu, K., Dong, J., Feng, J., Yu, L., 2025. Modeling the interplay between regional heterogeneity and critical dynamics underlying brain functional networks. Neural Networks 184, 107100. doi:`10.1016/j.neunet.2024.107100`.

Zhao, M., Zhou, C., Chen, Y., Hu, B., Wang, B.H., 2010. Complexity versus modularity and heterogeneity in oscillatory networks: Combining segregation and integration in neural systems. Physical Review E 82. doi:`10.1103/physreve.82.046225`.
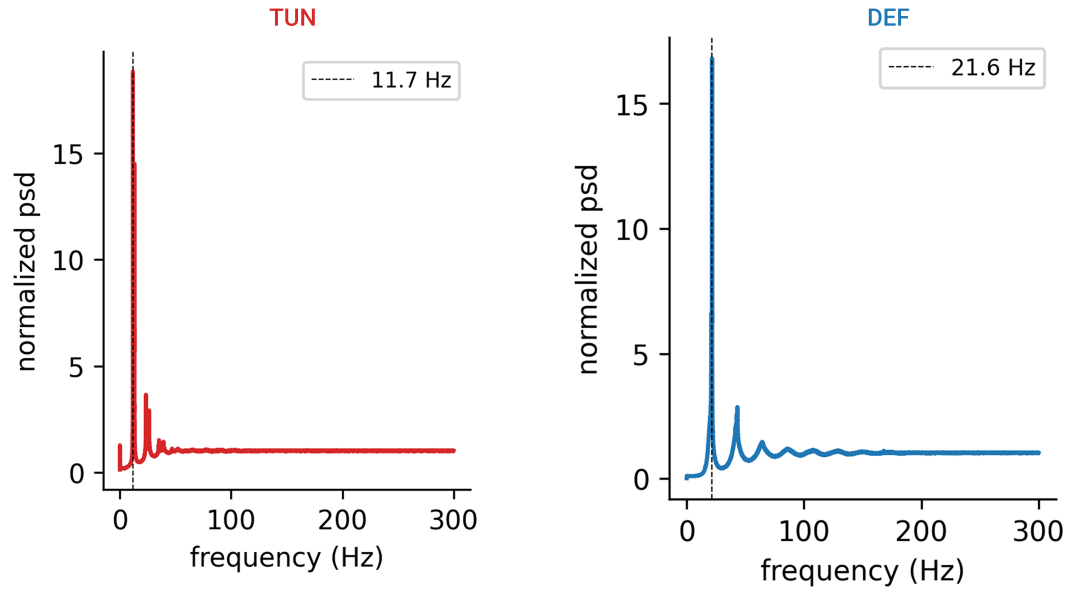
Supplementary Material

Figure A.1: **Power Spectral Density (PSD) of the events in TUN and DEF**.

PSDs were computed on the event time series for each node using the Welch method (with the same parameters as in Fig. 2), and were then averaged across nodes for TUN and DEF.
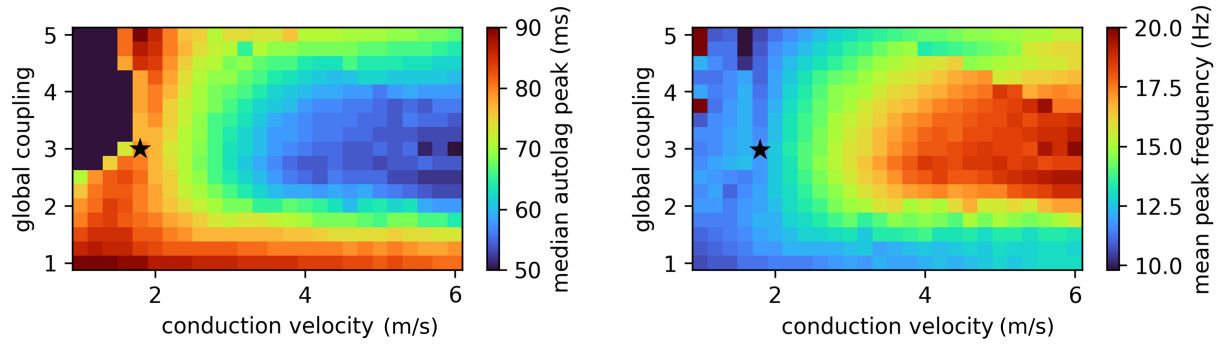
Figure A.2: **Global simulation parameters influence the global periodicity of the model**.
We varied the conduction velocity (from 1 to 6 m/s) and global coupling (from 1 to 5) and quantified the resulting changes in the median auto-correlation peak (second mode), for simulations obtained with TUN settings for the model. These manipulations induced variations in periodicity: higher conduction velocities were associated with faster periodicities (i.e., shorter median lags) across different global coupling values. The star identifies the pair of values used for simulations in this work.
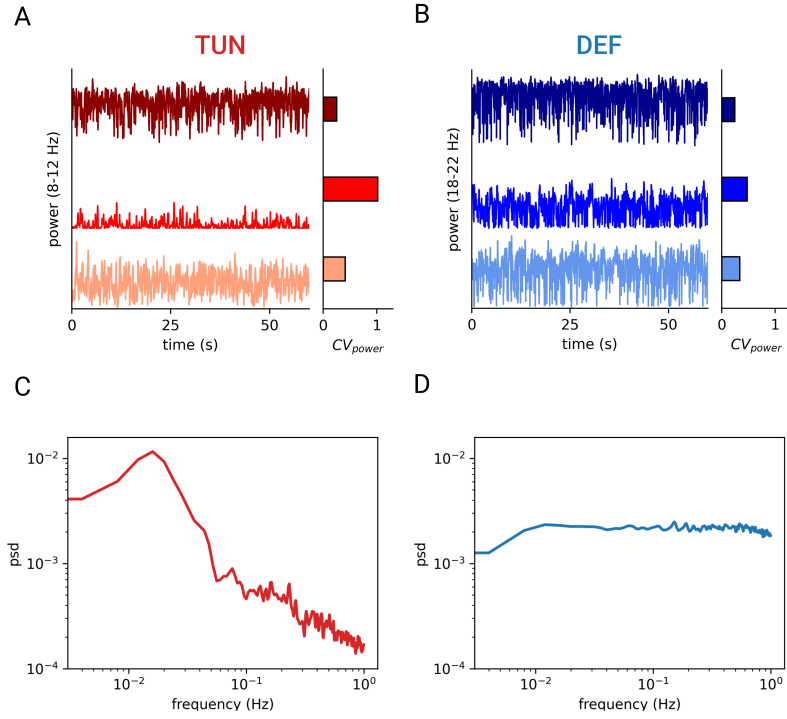
Figure A.3: **Power fluctuations over time in TUN and DEF**.

A) Time-frequency decomposition of power fluctuations using Morlet wavelet convolution. Power time-course (summed over the 8–12 Hz band) are shown for three representative nodes from Fig. 2 in TUN, together with the CV_{power} of each trace. **B)** Power traces in DEF as in A), but in the frequency range from 18 to 22 Hz. **C)** PSD of the power time-course for TUN computed using Welch method with time segments of 140 s and a 50 % overlap. **D)** PSD of the power time-course for DEF as in C).
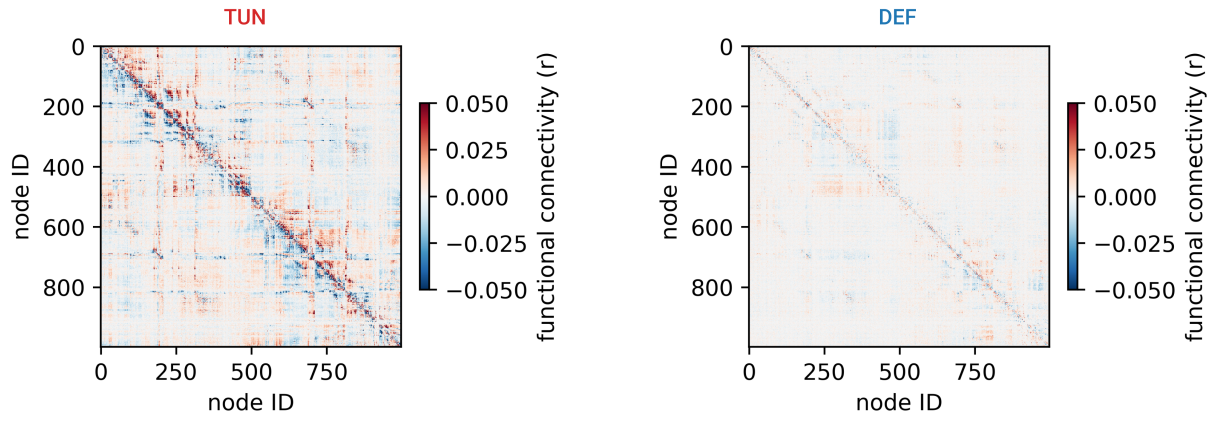
Figure A.4: **Functional connectivity asymmetry matrix ($\mathbb{FC}_{\mathrm{asym}}$) in the TUN and DEF configurations**.

The $\mathbb{FC}_{\mathrm{asym}}$ was quantified as $\mathbb{FC}_{\mathrm{asym}} = \mathbb{FC} - \mathbb{FC}^{\mathsf{T}}$, where $(\cdot)^{\mathsf{T}}$ denotes the matrix transpose. Positive values in $\mathbb{FC}_{\mathrm{asym},ij}$ indicate that node i has a stronger influence on node j than vice versa; negative values indicate the opposite.
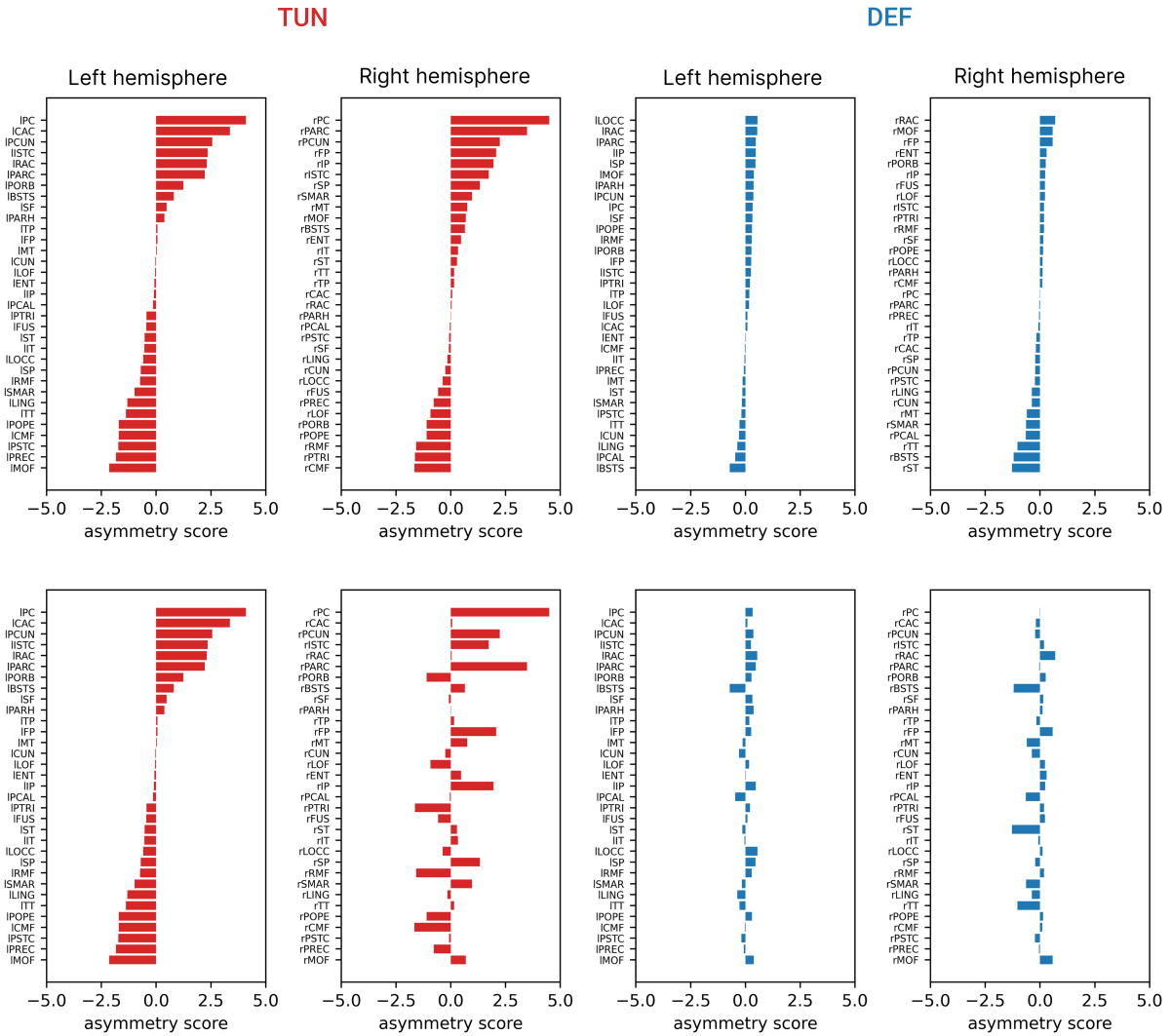
Figure A.5: **Average asymmetry score of each cortical region in TUN and DEF**.
Values for listed regions are obtained averaging the asymmetry score across the nodes located in the given region. In the top panels regions are sorted in their respective descending order. In the bottom panels regions are sorted in descending order according to the values of the first panel (left hemisphere of the TUN configuration).

Figure A.6: **Relationship between the asymmetry score and power fluctuations (CV_{power}) in DEF configuration**.

Linear regression shows a non-significant correlation ($r = 0.009$, $p = 0.77$).

Table A.1: **List of cortical regions and number of associated nodes.**
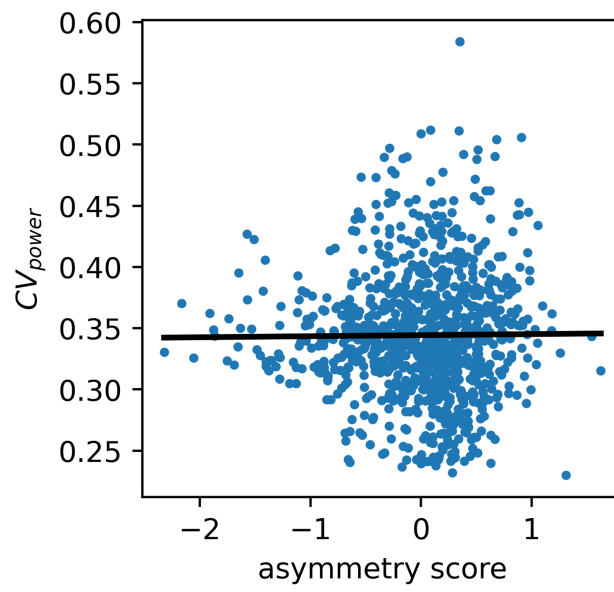Node counts are reported separately for the left and right hemispheres. The stimulated region (SP, superior parietal cortex, right hemisphere) is highlighted in bold, with the 27 nodes within this region stimulated simultaneously.

Label	Description	Number of nodes	
		Left	Right
BSTS	Bank of the superior temporal sulcus	5	7
CAC	Caudal anterior cingulate cortex	4	4
CMF	Caudal middle frontal cortex	13	13
CUN	Cuneus	8	10
ENT	Entorhinal cortex	3	2
FP	Frontal pole	2	2
FUS	Fusiform gyrus	22	22
IP	Inferior parietal cortex	25	28
IT	Inferior temporal cortex	17	19
ISTC	Isthmus of the cingulate cortex	8	8
LOCC	Lateral occipital cortex	22	19
LOF	Lateral orbitofrontal cortex	20	19
LING	Lingual gyrus	16	17
MOF	Medial orbitofrontal cortex	12	12
MT	Middle temporal cortex	19	20
PARC	Paracentral lobule	11	12
PARH	Parahippocampal cortex	6	6
PCAL	Pericalcarine cortex	9	10
POPE	Pars opercularis	11	10
PORB	Pars orbitalis	6	6
PTRI	Pars triangularis	7	8
PSTC	Postcentral gyrus	30	31
PC	Posterior cingulate cortex	7	7
PREC	Precentral gyrus	36	36
PCUN	Precuneus	23	23
RAC	Rostral anterior cingulate cortex	4	4
RMF	Rostral middle frontal cortex	19	22
SF	Superior frontal cortex	50	46
SP	**Superior parietal cortex**	27	**27**
ST	Superior temporal cortex	29	28
SMAR	Supramarginal gyrus	19	16
TP	Temporal pole	4	3
TT	Transverse temporal cortex	4	3

Table A.2: **TVB + Larter & Breakspear parameters**.

DEF column contains the default parameters of the LB model in TVB, taken from Alstott et al. (2009); TUN column reports the parameters of the tuned configuration. Parameter values that differ between the two configurations are indicated in bold. The parameters in the first block of the table refer to TVB simulator in general, while the second ones refer to the LB model specifically; notice the rescaling of some TVB general parameters, solely due to the time rescaling in the LB model.

Parameter	Description	Values	
		TUN	DEF
G	**Global coupling strength**	**3**	**1**
c_v	**Conduction velocity**	$\mathbf{3 \cdot t_{scale}}$	$\mathbf{3 \cdot t_{scale}}$
ξ	**Heun integrator noise**	$\mathbf{10^{-7} \cdot t_{scale}}$	$\mathbf{10^{-7} \cdot t_{scale}}$
t_{scale}	**Time scale factor**	**0.6**	**1**
V_{Ca}	**Ca Nernst potential**	**1.1**	**1.0**
$a_{e \rightarrow e}$	**Excitatory-to-excitatory synaptic strength**	**0.5**	**0.4**
g_K	**Conductance of K channels population**	**2.5**	**2.0**
g_L	**Conductance of leak channels population**	**1.1**	**0.5**
$a_{n \rightarrow i}$	**Non-specific-to-inhibitory synaptic strength**	**L: 0.4023; R: 0.4**	**0.4**
T_{Na}	**Threshold potential for Na channels**	**0.26**	**0.30**
δ_K	**Variance of K channels threshold**	**0.4**	**0.3**
V_T	**Threshold potential for excitatory neurons**	**-0.1**	**0.0**
δ_Z	**Variance of inhibitory threshold**	**0.60**	**0.65**
g_{Ca}	Conductance of population of Ca channels	1.1	1.1
r_{NMDA}	Ratio of NMDA to AMPA receptors	0.25	0.25
g_{Na}	Conductance of population of Na channels	6.7	6.7
V_{Na}	Na Nernst potential	0.53	0.53
V_K	K Nernst potential	-0.7	-0.7
V_L	Nernst potential of leak channels	-0.5	-0.5
$a_{i \rightarrow e}$	Inhibitory-to-excitatory synaptic strength	2.0	2.0
$a_{n \rightarrow e}$	Non-specific-to-excitatory synaptic strength	1.0	1.0
I	Subcortical input strength	0.3	0.3
b	Time constant scaling factor	0.1	0.1
$a_{e \rightarrow i}$	Excitatory-to-inhibitory synaptic strength	1.0	1.0
T_{Ca}	Threshold potential for Ca channels	-0.01	-0.01
T_K	Threshold potential for K channels	0	0
δ_{Ca}	Variance of Ca channels threshold	0.15	0.15
δ_{Na}	Variance of Na channels threshold	0.15	0.15
ϕ	Temperature scaling factor	0.7	0.7
τ_K	Time constant for K relaxation time	1	1
$Q_{V_{max}}$	Max firing rate for excitatory populations	1	1
δ_V	Variance of excitatory threshold	0.65	0.65
$Q_{Z_{max}}$	Max firing rate inhibitory populations	1	1
Z_T	Threshold potential for inhibitory neurons	0	0
C	Strength of excitatory coupling and balance between internal and global dynamics	0.1	0.1